

OBSERVING THE SEA SPRAY AEROSOL SIZE DISTRIBUTION ON THE
WINDWARD O'AHU COASTLINE

A THESIS SUBMITTED TO THE GRADUATE DIVISION OF THE
UNIVERSITY OF HAWAI'I AT MĀNOA IN PARTIAL FULFILLMENT OF
THE REQUIREMENTS FOR THE DEGREE OF

MASTER OF SCIENCE
IN
ATMOSPHERIC SCIENCES

May 2020

By
Chung Taing

Thesis Committee:
Alison D. Nugent, Chairperson
Jennifer D. Griswold
Steven G. Howell

Copyright
2020 by
Chung Taing

Acknowledgements

This material is based upon work supported by the National Science Foundation under EAGER Grant No. 1762166. Any opinions, findings, and conclusions or recommendations expressed in this material are those of the author and do not necessarily reflect the views of the National Science Foundation.

I would like to thank Alison Nugent for the opportunity to work with her. She provided fantastic guidance and mentorship. She had immense flexibility and patience in dealing with the questions and concerns that I have had throughout this experience. Without her help, I would not be where I am today. I have learned so much from her.

I would also like to thank Jorgen Jensen for his part in the project. His great enthusiasm was infectious. His expertise was invaluable. He devoted a great amount of time to analyzing each sample we sent his way. Without his help, this project would not be possible.

I also want to thank Katie Ackerman. She helped us every time we went out into the field to sample. She always had ideas when we ran into obstacles, and she helped to fuel many good discussions. She has begun her own work with the instrument developed in this project, and I am happy to see her ideas come to fruition.

I would also like to thank Dr. Jennifer Griswold and Dr. Steve Howell, the other thesis committee members on this project. With their knowledge, they provided me with new perspectives to consider every time we discussed the project.

I also want to thank John Leeman, who helped build custom anemometers and calibrated them in his wind tunnel, and Taylor Jones, who played a major role in creating the initial design of the instrument developed in this project.

Finally, I want to thank my friends and family for all their support. Without their love and friendship, the last two years would have felt much longer.

Abstract

Sea spray aerosol (SSA) play a significant role in the local climatology of coastal areas by acting as giant cloud condensation nuclei (GCCN), which can accelerate warm rain initiation due to their hygroscopicity. However, there is great uncertainty in SSA size and quantity in the atmosphere, particularly for large particles that act as GCCN. In-situ observations of GCCN are particularly limited because of their low concentration and relatively large sizes ($r_d > 0.5 \mu\text{m}$). At NCAR, the Giant Nucleus Impactor (GNI) was developed to observe giant aerosol particles. Optical microscope observations are made of wetted salt particles impacting onto polycarbonate slides exposed to ambient airflow in marine environments. With the GNI in mind, a new, low-cost, and accessible method for sampling large SSA in the marine boundary layer was developed. Using 3D printing and Arduino microcontrollers and sensors, a SSA sampler called the “mini-GNI” was designed and built that can expose slides to capture large and wet SSA. The mini-GNI can be attached to a kite string, allowing for sampling at multiple altitudes simultaneously. With the mini-GNI deployed on a kite platform, the SSA size distribution was observed on the windward side of O’ahu along with environmental variables that influence the SSA size distribution in the atmosphere. It was found that SSA concentration is not correlated with instantaneous wind speed as is usually expected over the open ocean. Instead, correlations were identified between SSA concentration and wave height as well as SSA concentration and wind history. These results suggest that the SSA present in the atmosphere in Hawai’i is locally generated by wave breaking along the coastline.

Table of Contents

Acknowledgements.....	3
Abstract.....	4
Table of Contents.....	5
List of Figures.....	7
List of Tables.....	10
Chapter 1: Introduction.....	11
1.1 Background.....	11
1.2 Importance of SSA.....	12
1.3 Characterization of SSA.....	15
1.4 External Impactor Method.....	17
1.5 Study objectives.....	22
Chapter 2: Methodology.....	23
2.1 Instrument Design.....	23
2.1.1 Mini-GNI.....	23
2.1.2 Anemometer.....	25
2.2 Kite Sampling and Environmental Data.....	26
2.3 Microscope Analysis.....	28
2.4 Environmental Variables.....	31
2.4.1 Relative Humidity.....	31
2.4.2 Wind Speed Aloft.....	32
2.4.3 Other Variables.....	33
Chapter 3: Results.....	34
3.1 Altitude.....	35
3.2 Wind Speed.....	37
3.3 Wave Height.....	38
3.4 Wind History.....	39
Chapter 4: Discussion and Conclusions.....	41
4.1 Local Production of SSA.....	41
4.2 Local Factors.....	44
4.3 Lognormal Distribution Fitting.....	48
4.4 Wind Sensitivity Study.....	51

4.5 Other Uncertainties	54
4.5.1 Relative Humidity	54
4.5.2 Orientation	56
Chapter 5: Summary and Conclusions	58
Chapter 6: References	60
Chapter 7: Appendix	65
7.1 Mini-GNI 3D Design	65
7.2 Mini-GNI Assembly.....	66
7.3 Mini-GNI Software	72

List of Figures

Figure 1. The solid and empty circles represent the growth and evaporation, respectively, of SSA droplets represented as a Particle Mass Change w/w_0 showing the mass (w) with respect to the initial mass when dry (w_0) as a function of RH (%). The dashed line represents the same for pure NaCl particles. Figure 1 from Tang et al. (1997).

Figure 2. Observations of SSA on O'ahu using the external impactor method: a) Cumulative SSA concentration (m^{-3}) by wind force and b) Cumulative concentration (m^{-3}) by altitude (m) is plotted against particle radius at 99% RH and by weight of sea salt particles (μg). Figures 1 and 5 from Woodcock (1953), respectively.

Figure 3. The average variation of SSA mass concentration ($\mu\text{g m}^{-3}$) with height (10^2 m) found from the external impaction method. Figure 5 from Blanchard et al. (1984).

Figure 4. The average variation of sea salt mass concentration ($\mu\text{g m}^{-3}$) with height (m) from four locations: Bellows beach, Kahuku beach, Kahuku inland, and Bellows ocean. Figure 9 from Daniels (1989).

Figure 5. Image of a polycarbonate slide. The flat center area is used for sampling and has a length of 20.7 mm and a width of 4.4 mm.

Figure 6. An image of a portion of a slide taken by the optical microscope. The grid spacing is $37 \mu\text{m}$. 350 images are taken per slide. Two arrows point towards two droplets, which are flatter due to reduced surface tension, possibly due to containing organics, resulting in lighter coloring. Figure 4 from Jensen et al. (2020a).

Figure 7. A photograph of the mini-GNI with its door open showing the exposed polycarbonate slide on the instrument's arm.

Figure 8. A photograph of the touchscreen control station used to communicate with the mini-GNI instrument from the ground while the mini-GNI is aerially deployed.

Figure 9. A photograph of the custom anemometer. The wing on the left orients the fan (offwhite color object at top) in the direction of the wind. The Adafruit FeatherWing electronics are visible inside the anemometer housing.

Figure 10. A map of O'ahu marked with important locations relevant to this study: the red box indicates the sampling location from Kaupo Bay, the green box indicates the buoy location, the purple box indicates the Marine Corps Air Station, and the orange box indicates the NWLON station. Map from Google Maps (2019).

Figure 11. A photograph of a mini-GNI instrument attached with a carabiner to the kite string using a black zip tie. Notice that the door is closed until the instrument reaches the desired altitude, and an orange streamer is also attached for visibility.

Figure 12. A cartoon of the sampling setup for 9/10/19. The iMet-XQ2 instrument is at the top, followed by a number of mini-GNI instruments. The altitude levels are averaged from three samples at each altitude from 9/10/19. The spacing between each mini-GNI is ~ 150 m.

Figure 13. CE (line and color contours) is plotted as a function of SSA dry radius (μm) and wind speed (m s^{-1}).

Figure 14. Same as Figure 13, but zoomed into $1\text{-}5 \mu\text{m}$ dry radius and $1\text{-}5 \text{m s}^{-1}$ wind speed with labeled line contours of CE.

Figure 15. The RH (color) for each sample plotted for each date at the average sampling altitude. RH was estimated for all samples on 12/1/18 and 1/1/19 and for 3 samples on 4/13/19 and 4/23/19. It was observed for all other samples.

Figure 16. SSA size distributions fitted to lognormal distributions from a) VOCALS-REx off the coast of Peru and Chile using the aircraft-deployed GNI, and b) this study along the coastline of O'ahu using the kite-deployed mini-GNI. The bins for both studies are identical with a bin size width of 0.2 μm .

Figure 17. a) The cumulative number concentration of SSA (m^{-3}) on a log scale is plotted against the dry radius bins of the size distribution (μm). Each line represents a different sample and is colored by the mean altitude of the sample. b) The total number concentration (m^{-3}) is plotted against altitude (m). Each scatter point is sized by the significant wave height (m) and colored by the surface wind speed (m s^{-1}) observed during the sample time.

Figure 18. For each sampling day with more than 2 samples, the cumulative number concentration (m^{-3}) is plotted against dry radius bins (μm) of the size distribution. Each line represents a different sample and is colored by the mean altitude during sample collection. The sampling days with more than 2 samples are a) 12/5/18, b) 1/1/19, c) 4/13/19, d) 4/23/19, e) 7/31/19, f) 8/15/19, g) 8/20/19, h) 8/22/19, and i) 9/10/19.

Figure 19. a) The cumulative number concentration (m^{-3}) in log scale is plotted against the dry radius bins (μm) of the size distribution. Each line represents a different sample and is colored by the mean surface wind speed (m s^{-1}) that the sample was taken at. Dashed lines, categorized by wind speed (m s^{-1}), are used to represent data from Woodcock (1953). b) The total number concentration (m^{-3}) is plotted against surface wind speed (m s^{-1}). Each scatter point is sized by the significant wave height (m) and colored by the altitude (m) observed during the sample time.

Figure 20. a) The cumulative number concentration (m^{-3}) on a log scale is plotted against the dry radius bins of the SSA size distribution (μm). Each line represents a different sample, and is colored by the significant wave height (m) observed during the sampling time. b) The total concentration for each sample (m^{-3}) is plotted against significant wave height (m). Each scatter point is sized by the surface wind speed (m s^{-1}) and colored by the average altitude of the sample (m).

Figure 21: Total SSA number concentration (m^{-3}) is plotted against a) Instantaneous surface wind speed (m s^{-1}), b) 12-hour mean wind prior to sampling (all m s^{-1}), c) 24-hour mean wind prior to sampling, d) 48-hour mean wind prior to sampling. Scatter points are sized by the wave height (m) and colored by the average altitude (m) at which the sample was collected.

Figure 22. HySPLIT 60-hour back trajectories for sampling days a) 12/5/18, b) 1/1/19, c) 4/13/19, d) 4/23/19, e) 7/31/19, f) 8/15/19, g) 8/20/19, h) 8/22/19, i) 9/10/19. The green, blue, and red colors represent low, medium, and high altitude respectively, ranging from near-surface (~25 meters) to ~750 meters. Each point on the trajectory line marks a 6 hour interval.

Figure 23. Dry deposition residence times for SSA based on r_{∞} . Figure taken from Lewis and Schwartz (2004), their Table 8.

Figure 24. Topography and bathymetry (color) of a) O'ahu, b and c) the sampling site, with overlaid flight paths showing the exact location of sampling. A thick black line marks the 0 m contour, outlining the coastline.

Figure 25. The total number concentration (m^{-3}) is plotted against tide level (m). Each scatter point is sized by the wave height (m) and colored by the average altitude (m) where the sample was collected.

Figure 26. Two examples of SSA size distribution fit with the lognormal distribution from a) 4/13/19 and b) 8/22/19. Listed on each distribution plot are the geometric mean dry radius (μm), the geometric standard deviation, the χ^2 value of the fit, and the p-value of the fit.

Figure 27. The distributions for total salt mass (top row), geometric mean radius (middle row), and geometric standard deviation (bottom row) observed over the open ocean by the GNI during VOCALS-REx (left column) and along the O'ahu coastline by the mini-GNI (right column).

Figure 28. Vertical wind profile (all m s^{-1}) of observation data from two anemometers (green and blue dots) are plotted along with the power law wind profile and a log law wind profile fitted to the observation data.

Figure 29. Descriptions of various roughness parameter, z_0 (m), values are given for use in the log law estimation for wind profiles. Figure 10.5 from Arya (2001).

Figure 30. a) The effect of changing wind speed on an example SSA size distribution. In blue is the original size distribution and in red is the effect of decreasing the wind estimate by 35%. b) The ratio of the concentration calculated from decreasing wind by 35% to the observed concentrations (red vs blue histogram in a) is plotted.

Figure 31. Relaxation time (s) for drop radius (red), drop temperature (blue), and drop inertia (cyan) is plotted as a function of the drop's initial radius, r_0 (μm). Figure 4 from Veron (2015).

Figure 32. The three stages of Euler angle rotation: a) Φ , b) θ , and c) Ψ . Figure 1 from Schwab and Meijaard (2006).

Figure 33. Rose plots of the alpha, beta, and gamma orientation angles corresponding to Φ , θ , and Ψ Euler angles for two samples on a) 4/13/19 at 275 m and b) 7/31/19 at 431 m.

Figure A1. The 3D design of the mini-GNI instrument from a) the side, and from b) the top. Both views are slightly angled for better visualization, but the length measurements are flat.

Figure A2. The Micro Servo and the Feather M0 are placed into position. The Adalogger FeatherWing and the MPL3115A2 are wired but not put in place.

Figure A3. The Adalogger FeatherWing has been attached to the Feather M0.

Figure A4. The MPL3115A2 sensor has been placed into position.

Figure A5. The SPDT slide switch used to power the instrument on and off has been put into place.

Figure A6. The arm is put in place with the spring, clevis, and cotter pin.

Figure A7. The batteries are put in place. Note that this version of the mini-GNI does not have a BNO055 sensor, which would be placed just above the MPL3115A2 sensor.

Figure A8. The door is screwed into place to the Micro Servo. The AM2302 sensor is attached to the side via adhesive putty as seen in Figure 5.

Figure A9. The software logic diagram for the mini-GNI. Every ~2-3 seconds, the mini-GNI reads sensor data and saves it. It also sends data for viewing to the ground control station. If it receives a message from the user at the control station, it opens and closes its door to expose and withdraw the polycarbonate slide for SSA impaction.

Figure A10. The software logic diagram for the mini-GNI control station. It receives information from the mini-GNI and displays it on the touchscreen. If the "open" or "close" commands are touched, the control station sends a message to the mini-GNI ordering it to open or close.

List of Tables

Table 1. The difference in CE between particles at equilibrium (with 80% RH) radius and at formation radius.

Table A1. Adafruit parts list for building the mini-GNI.

Table A2. Adafruit parts list for building the mini-GNI control station.

Chapter 1: Introduction

1.1 Background

Sea salt aerosols (SSA) are a natural aerosol predominant in the marine boundary layer (MBL) and widely distributed throughout Earth's atmosphere. SSA are relatively large aerosols, falling under the coarse aerosol size range (1-40 μm). They are primarily composed of sodium chloride (NaCl). Due to their salt content, SSA are hygroscopic, and absorb moisture easily. For example, at equilibrium with 80% relative humidity (RH), SSA can grow to 4 times their dry mass (Tang et al. 1997).

SSA come from sea spray and are primarily formed via wave breaking. In the open ocean, waves break under high wind conditions ($>4 \text{ m s}^{-1}$), while in coastal surf zones, waves break upon interaction with coastal bathymetry and reefs. SSA enter the atmosphere through bubbles bursting, jet drop ejection, and spume drops due to wind-wave interaction (de Leeuw et al. 2011). These processes create three different sizes of SSA: film drops (dry radius or $r_d < 0.5 \mu\text{m}$), jet drops ($0.5 < r_d < 12 \mu\text{m}$), and spume drops ($r_d > 12.5 \mu\text{m}$) described as follows. When waves break, air is entrained into the water in the form of bubbles. The bubbles rise to the ocean surface and burst, forming whitecaps. When a bubble initially bursts, the film of the bubble is broken apart into film drops ($r_d < 0.5 \mu\text{m}$), which are ejected into the atmosphere. Due to their small size, they do not readily undergo dry deposition, or settling by gravity. For example, the residence time due to dry deposition of a SSA particle with $0.5 \mu\text{m}$ dry radius is 1.5 weeks (Lewis and Schwartz 2004). Film drops are instead primarily removed from the atmosphere through wet deposition, or rain.

After a bubble bursts, a cavity is left behind in place of the bubble. Water rushes in to fill the cavity, which collides and results in a vertical jet of water that shoots upward. The jet then breaks up into jet drops ($0.5 < r_d < 12 \mu\text{m}$), which are ejected into the atmosphere. Because of their heavier weight, jet drops are primarily removed from the atmosphere by dry deposition. It follows that the larger the jet drop, the more quickly it settles due to gravity. For example, the residence time of a $5 \mu\text{m}$ dry radius SSA is 5 hrs while that of a $10 \mu\text{m}$ SSA is just 15 mins (Lewis and Schwartz 2004).

Finally, if the wind is strong enough, it can tear large spume drops ($r_d > 12.5 \mu\text{m}$) off of the wave crest. Due to their large size, spume drops are quickly removed by dry deposition in seconds or minutes (Lewis and Schwartz 2004). Because spume drops are too big to remain in the atmosphere and film drops are too small for our methodology to observe, this study focuses on the SSA size range associated with jet drops.

1.2 Importance of SSA

SSA are an important aerosol in the MBL, and are dominant with respect to their mass. They play several roles in the atmosphere in chemical, radiative, and cloud processes, some of which are described as follows.

SSA are an important participant in tropospheric chemistry as the largest source of tropospheric bromine (Parrella et al. 2012). Bromine radicals can deplete ozone and OH radicals in the troposphere, affecting the lifetime of several compounds, including the greenhouse gas methane. Additionally, bromine radicals oxidize elemental mercury, which can lead to quicker deposition of mercury to the Earth's surface in more toxic forms (Saiz-Lopez and von Glasow 2012). Knowing the quantity of SSA in the troposphere is therefore important for understanding the global budget of tropospheric bromine and oxidants.

SSA contribute to the radiation budget of the atmosphere via the aerosol direct effect. SSA scatter radiation affecting visibility and radiative forcing. SSA with dry radius $< 2.5 \mu\text{m}$ contribute significantly to the direct effect (McNaughton et al. 2007) while larger SSA contribute to radiative forcing through the aerosol indirect effect (Twomey 1997) by acting as cloud condensation nuclei (CCN), or a surface on which cloud water can condense. A large (small) amount of CCN can lead to greater (lower) scattering of radiation and an extended (shortened) lifetime of clouds, resulting in higher (lower) cloud albedo and a longer (shorter) cloud lifetime. Accurate knowledge of SSA is essential for the ability to define a base case of radiative forcing in the absence of anthropogenic aerosols, and knowledge of the baseline can then be used to assist in evaluating the effect of anthropogenic aerosols on radiative forcing and climate (IPCC 2013). Furthermore, knowledge of SSA naturally occurring in the atmosphere allows for a more accurate representation of these radiative and cloud modifying impacts of SSA, ultimately leading to a more complete understanding of weather and climate change when incorporated into numerical models.

Large SSA ($r_d > 0.5 \mu\text{m}$) can act as giant CCN (GCCN), hypothesized to accelerate warm rain initiation (Jensen and Nugent 2017) due to their high salt content and resulting high hygroscopicity (Tang et al. 1997). Figure 1 shows the wetting that sea salt particles experience beginning at $\sim 70\text{-}74\%$ RH; by 90% RH, sea salt particles have a mass approximately eight times that of their dry mass due to the addition of water (Tang et al. 1997). In the MBL, humidity typically remain high, so most SSA stay on the droplet evaporation curve in Figure 1 for their entire existence since they form at near 100% humidity.

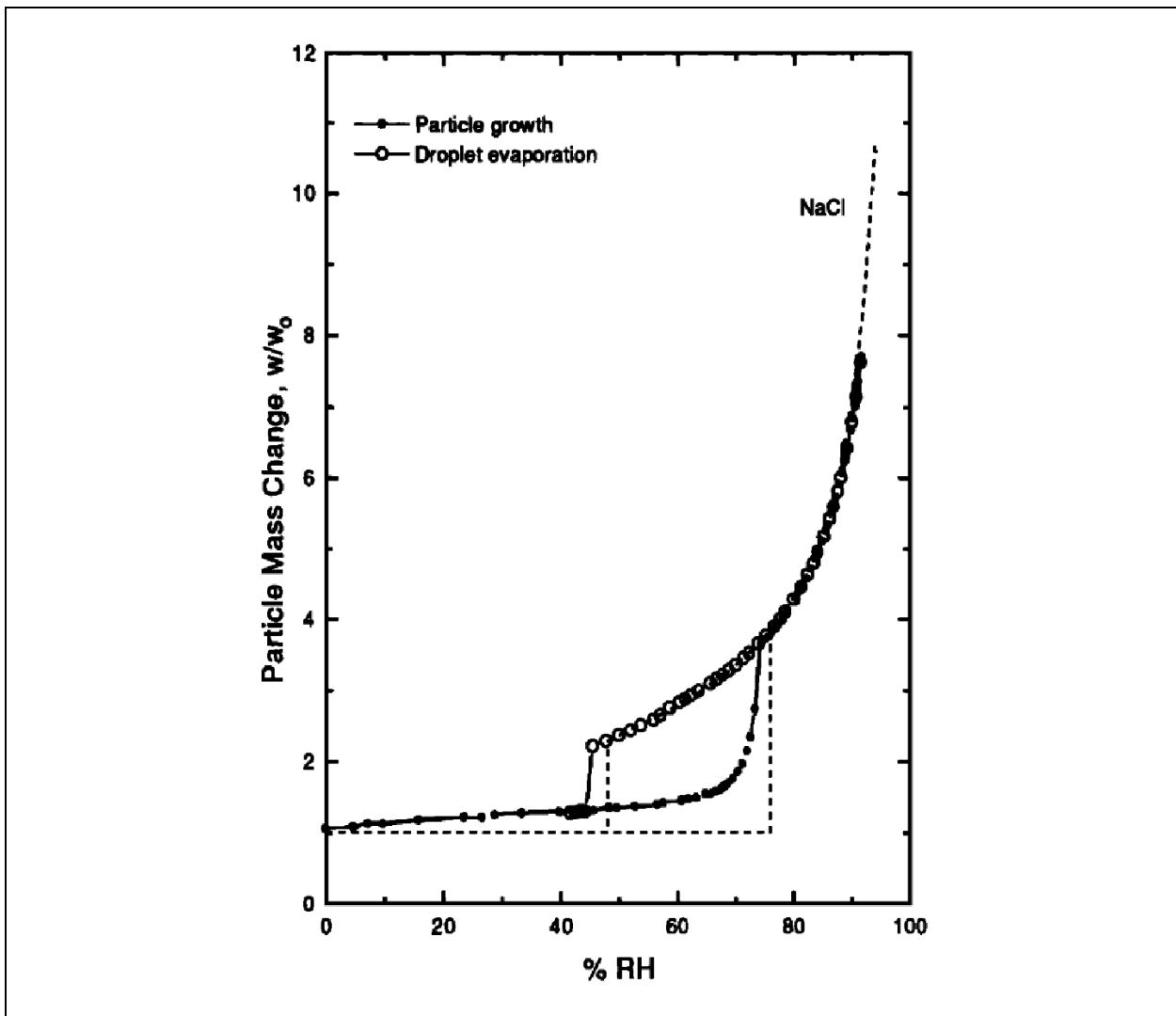


Figure 1: The solid and empty circles represent the growth and evaporation, respectively, of SSA droplets represented as a Particle Mass Change w/w_0 showing the mass (w) with respect to the initial mass when dry (w_0) as a function of RH (%). The dashed line represents the same for pure NaCl particles. Figure 1 from Tang et al. (1997).

Jensen and Nugent (2017) show that droplets grown on GCCN with $r_d > 2 \mu\text{m}$ remain concentrated salt solutions and have accelerated condensational growth as compared to pure liquid water drops when lifted in identical environments. There is an extensive history of work related to SSA and to GCCN, which sets the stage for this research. A subset of the prior research is summarized as follows.

SSA were first suggested to act as GCCN by Houghton (1938), who proposed that low lying large hygroscopic nuclei can grow into large drops for rapid coalescence. Johnson (1982) used a condensation model to track “the evolution of several hundred categories of condensation nuclei of variable size and solubility from ~400 m below cloud base (80% relative humidity) to 500 m above cloud base” (Johnson 1980), finding that ultragiant particles (defined by Johnson 1982 as “aerosol particles larger than $10 \mu\text{m}$ ”) do not even need to be soluble to initiate precipitation. Feingold et al. (1999) investigated GCCN with a variety of models, including a box model of collection, a trajectory ensemble model, a 2D eddy-resolving model, and a 3D large-eddy simulation model. They found that drizzle appears at the ground surface earlier when GCCN are present and that GCCN have the strongest impact on the collection process in cases where there is a high number of CCN present (Feingold et al. 1999). Khairoutdinov and Kogan (2000) found that clouds with low CCN and large drop sizes produce high drizzle rate and fast removal of CCN in a large-eddy simulation using their bulk microphysical parameterization. Blyth et al. (2003) compared observations of early radar echoes in small cumulus clouds to a stochastic coalescence model, finding that ordinary collision and coalescence by giant and ultragiant nuclei are a reasonable explanation for early radar echoes. Jensen and Lee (2008) concluded from a study using a stochastic Monte Carlo cloud model that SSA effects should be included in the parameterization of warm rain formation since large SSA determine the rainfall rate once wind speeds exceed $4\text{-}5 \text{ m s}^{-1}$. Watson et al. (2015) offered SSA cloud microphysical effects as one of several hypotheses for the sharp reduction of precipitation observed on a tropical island when winds are weak. Finally, Jensen and Nugent (2017) used a droplet growth model, which included the solute and surface tension term, and found that SSA GCCN grow larger and more quickly than pure water droplets due primarily to the solute term in the drop growth equation, and therefore act to broaden the cloud droplet spectrum.

Further evidence that some form of acceleration of warm rain initiation is required can be found in mountainous regions where precipitation is formed due to the orographic effect. For orographic rain to occur, the time required for cloud droplets to grow to precipitation size can be very short depending on the terrain and the wind speed (Banta 1990). Mountain ranges with very broad uplift regions or slow wind speeds allow for sufficient time for microphysical processes to grow cloud and rain drops before air descends on the leeside. On the other hand, mountain ranges with narrow uplift regions or high wind speeds allow for less time. In general, the time available for microphysical processes to produce rain is between 30 minutes to 1 hour (Banta 1990). An extreme example lies in the Ko'olau Mountain Range on the Hawaiian Island of O'ahu (21.4389°N, 158.0001°W). The Ko'olau Range is narrow, and for precipitation to initiate after lifting begins, droplet growth from cloud droplet to rain drop size must occur in only 5 mins (Banta 1990). There must be a method for droplets to grow to precipitation size in only 5 mins, and a simple theoretical explanation is that SSA are large enough to act as GCCN, which grow to precipitation size within the allotted time.

The role that SSA play in chemistry, aerosol direct and indirect effects, and cloud microphysics depends on the size of the SSA particle. The size determines the lifetime of the aerosol in the atmosphere, and thus the amount of salt present. This in turn allows SSA particles of different sizes to contribute differently to a wide range of atmospheric processes. For these reasons, knowledge of the size distribution of SSA and how it changes with meteorological conditions and geographic location is critical (Lewis and Schwartz 2004).

1.3 Characterization of SSA

Despite their importance, SSA are poorly characterized. In an extensive review of SSA, Lewis and Schwartz (2004) state that uncertainties for studies regarding SSA are at the order of magnitude level. This isn't surprising given the difficulties involved in observing SSA.

When observing SSA, there is currently no method to determine the age of the aerosol. This is especially problematic because SSA take time to reach their equilibrium size, and the time depends on their individual r_d . If the age is unknown, then in many methods, it becomes impossible to calculate the equivalent dry size and a size distribution. This issue can be resolved by examining only a narrow range

of the size distribution. For example, if only SSA with $r_d < 12.5 \mu\text{m}$ are observed, then it can be assumed that they have already reached their equilibrium size (Lewis and Schwartz 2004). Similarly, if only SSA with $r_d > 25 \mu\text{m}$ are observed, then it can be assumed that they are at formation size. In both examples, these assumptions allow the real size to be discerned.

Additionally, large SSA ($r_d > 2.5 \mu\text{m}$) are not well characterized due to their naturally low concentration in the atmosphere, necessitating a large sample volume in observations. The size range of these large SSA lies in an awkward region where neither instruments built to study aerosols nor cloud droplets can be used.

Aerosol observing instruments that require the use of aircraft inlets cannot observe large SSA because inlets suffer from losses of larger particles. These losses are a result of impaction to the walls of the inlet due to the higher inertia of larger particles and due to turbulence in the inlet (McNaughton et al. 2007). McNaughton et al. (2007) compared three passive solid diffuser inlets in the DC-8 Inlet Characterization Experiment (DICE), finding that the 50% passing efficiency for the inlets was 3.1, 2.5, and 2.0 μm in geometric particle diameter. Because of these size limitations, there is a limited understanding of SSA particles with supermicron ($> 1.0 \mu\text{m}$) size.

Optical probes such as the Forward Scattering Spectrometer Probe (FSSP) do not require inlets and therefore can be used to observe large SSA. However, they are designed to observe cloud droplets and cannot distinguish between cloud droplets with or without salt or other CCN inside (Lasher-Trapp and Stachnik 2007). Optical instruments measure optical size, and therefore cannot distinguish between hygroscopic and non-hygroscopic particles, or determine what material may have initially acted as the CCN for a particular cloud droplet. Additionally, most optical instruments may incorrectly size non-spherical particles and cannot distinguish between spherical and non-spherical particles.

There are other methods of observing SSA, such as using air filters (Savoie and Prospero 1977), lidar remote sensing (Porter et al. 2000), a multijet cascade impactor or satellite remote sensing (Jaegle et al. 2011), and atomic emission spectroscopy of sodium (Campuzano-Jost et al. 2003). However, none can provide the size distribution of SSA. The only method with some success in sampling supermicron SSA that can also resolve the size distribution is the external impactor method.

1.4 External Impactor Method

The external impactation method was first used by Alfred Woodcock in the 1950s. He mounted glass slides coated with Dri-film on wind vanes and aircraft to collect water droplets, which impacted on the slides, leaving a hemispheric impression (Woodcock and Gifford 1949, Woodcock 1952). The slides were placed in a chamber with controlled temperature and humidity overnight, allowing the SSA to reach equilibrium size, before being manually analyzed by an optical microscope for SSA counts and diameters.

Woodcock performed his external impactor sampling at multiple locations, including off the coasts of windward O'ahu, Florida, and South Australia. Figure 2a and b provides an overview of SSA size distribution from O'ahu showing SSA concentration increasing with increasing wind force and with decreasing altitude respectively (Woodcock, 1953).

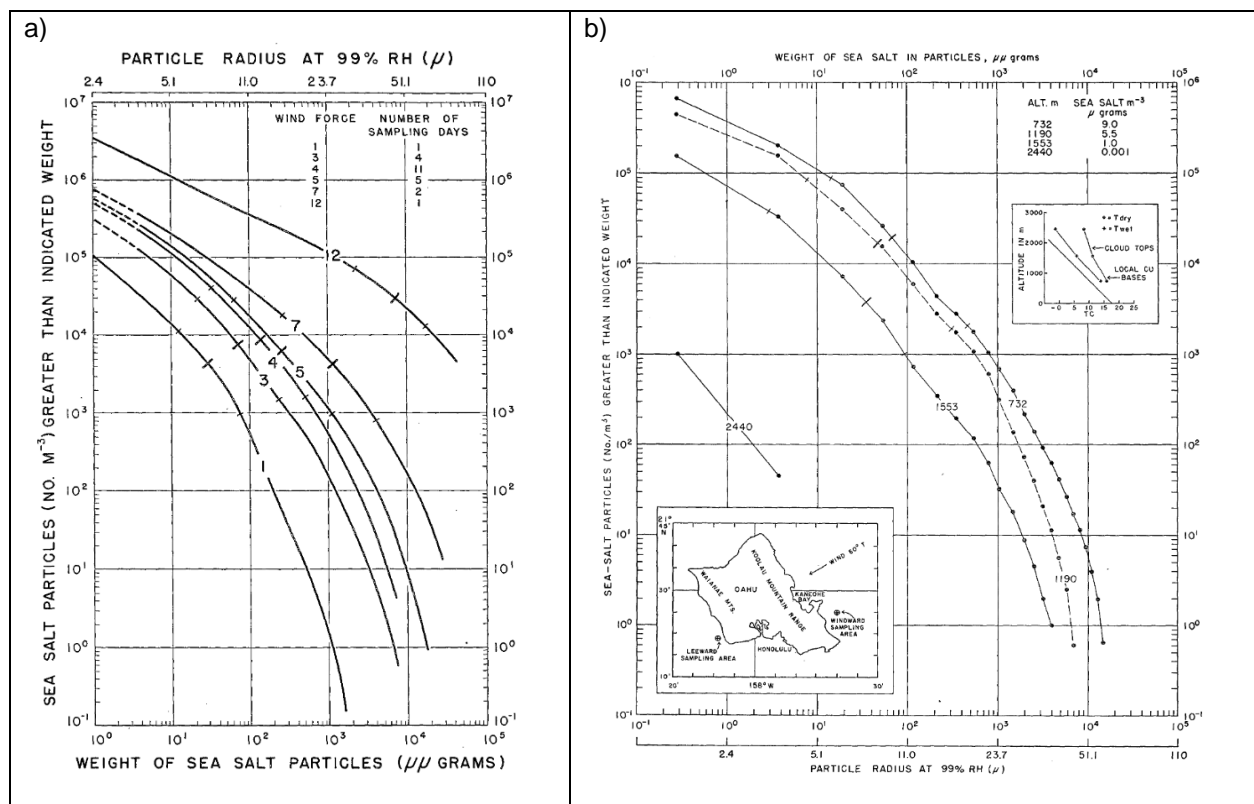


Figure 2: Observations of SSA on O'ahu using the external impactor method: a) Cumulative SSA concentration (m^{-3}) by wind force and b) Cumulative concentration (m^{-3}) by altitude (m) is plotted against particle radius at 99% RH and by weight of sea salt particles ($\mu\mu\text{g}$). Figures 1 and 5 from Woodcock (1953), respectively.

Blanchard et al. (1984) also sampled SSA windward of O'ahu using glass slides by flying an aircraft between ~30-1000 m altitude. SSA below 30 m along the coastline was also sampled using towers. The salt from the slides was washed with distilled water, and the resulting solute water drop was analyzed by flame atomic absorption spectroscopy for sodium concentration, which was then converted into total sea salt concentration. Blanchard et al. (1984) found a twofold decrease in average SSA amount was found between 19 and 30.5 m followed by a more gradual decrease with height (Figure 3).

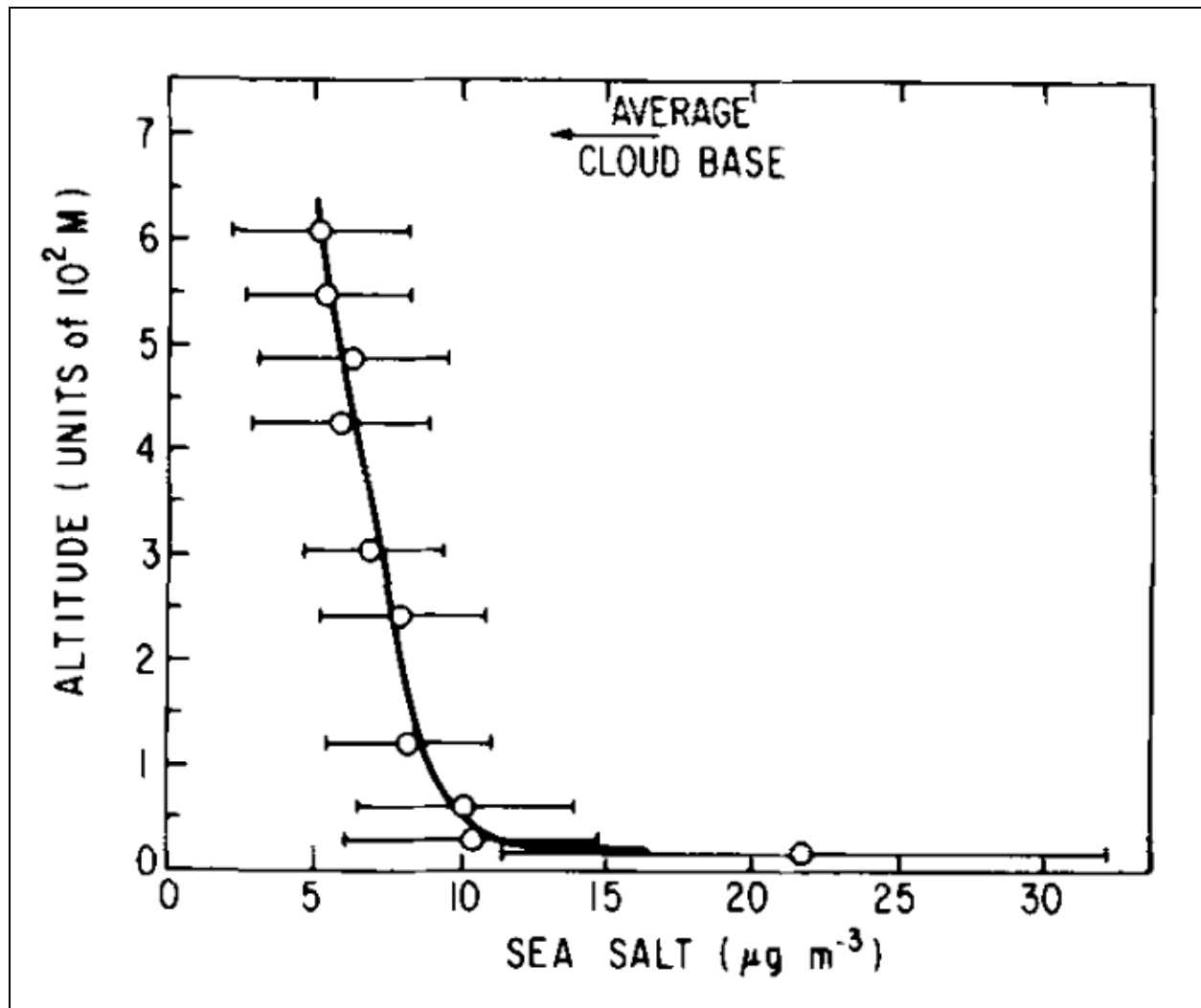
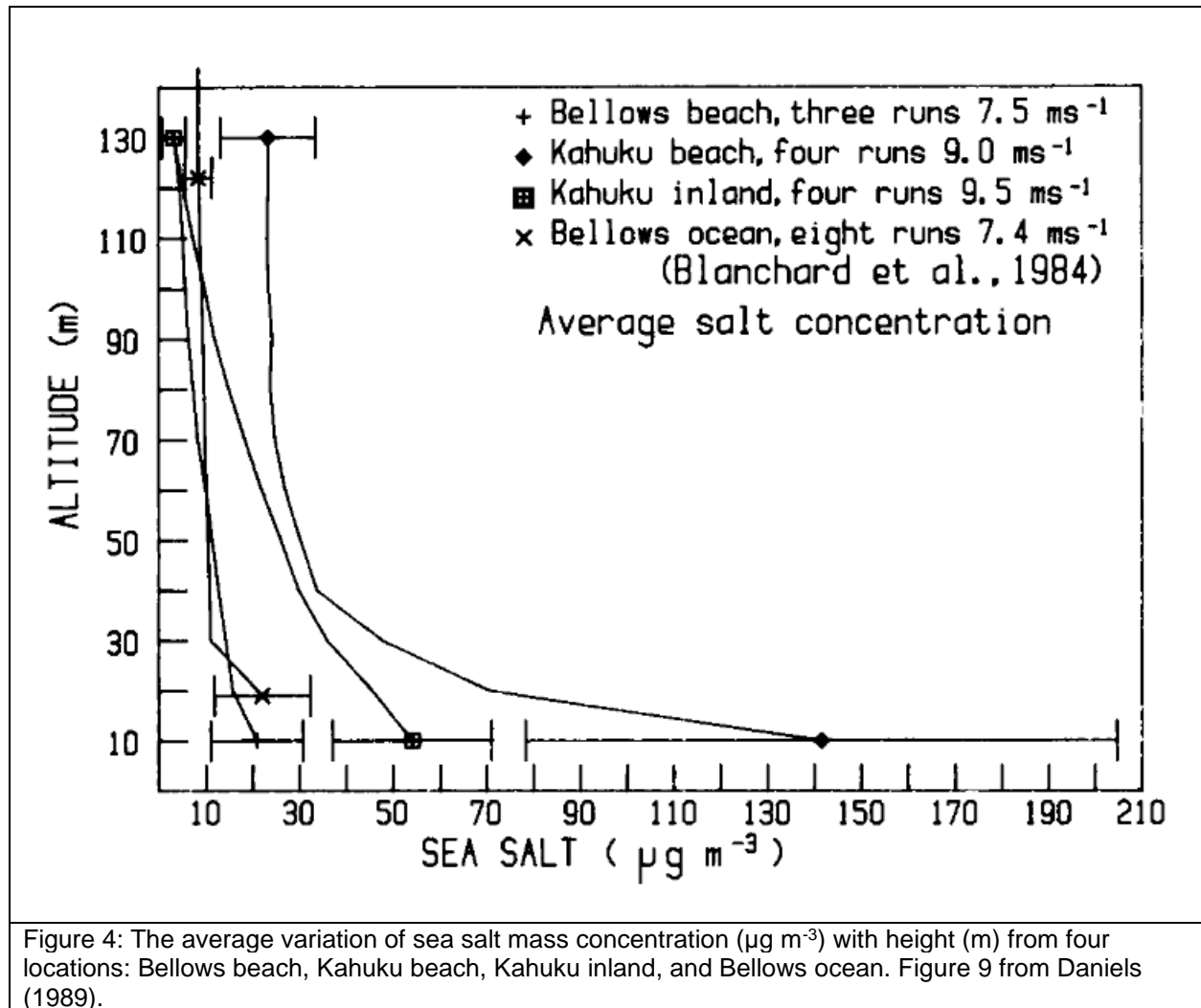


Figure 3: The average variation of SSA mass concentration ($\mu\text{g m}^{-3}$) with height (10^2 m) found from the external impaction method. Figure 5 from Blanchard et al. (1984).

Daniels (1989) also performed external impaction sampling but with steel wires along a kite string. The kite provided a cheap and convenient alternative to aircraft. After exposure, the steel wires were then rinsed, and analyzed with atomic absorption spectrometry in the same way as Blanchard et al. (1984).

Daniels (1989) also found a sharp decrease in concentration with height in the lowest 30 m of the atmosphere, though the decrease with height is more uniform inland far from the surf zone (Figure 4).



More recently, Jensen et al. (2020a) have developed another external impactation method called the Giant Nucleus Impactor, or GNI, which was used in the Variability of the American Monsoon Systems (VAMOS) Ocean-Cloud-Atmosphere-Land Study-Regional Experiment (VOCALS-REx) campaign. VOCALS-Rex observations were made over the ocean off the coast of Peru and northern Chile in the domain of 12° - 31° S and 69° - 86° W (Mechoso et al. 2014).

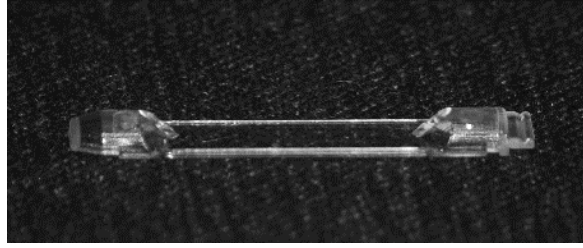


Figure 5: Image of a polycarbonate slide. The flat center area is used for sampling and has a length of 20.7 mm and a width of 4.4 mm.

Polycarbonate slides (Figure 5) are exposed from aircraft and then dried in desiccated tubes. For analysis, the slides are placed in a chamber with controlled temperature and humidity, and the SSA are allowed to reach their equilibrium size at 33.5 °C and 90% RH. Salt particles form spherical solution caps on the slide while other particles are unlikely to form circular drops, or may form circular drops with less defined edges when viewed from above (Figure 6). This method is therefore particularly good at distinguishing between hygroscopic and non-hygroscopic particles. An automated optical microscope then images all the slides, and software counts the spherical drops on the slides. A more extensive description of the GNI microscope and its software is given in Jensen et al. (2020a).

The raw count of SSA obtained by the software can then be converted to a number concentration given the sample volume (V_S) and collision efficiency (CE) of SSA particles impacting the slide:

$$N_{SSA} = \frac{N_{raw}}{V_S \cdot CE} \quad (\text{Eq. 1}).$$

The sample volume (V_S) is defined as the area of the slide multiplied by the sample duration and the wind speed. CE is calculated by considering particles impacting an infinitely long ribbon with finite width (Ranz and Wong 1952). The CE calculation is described further in Section 2.3.

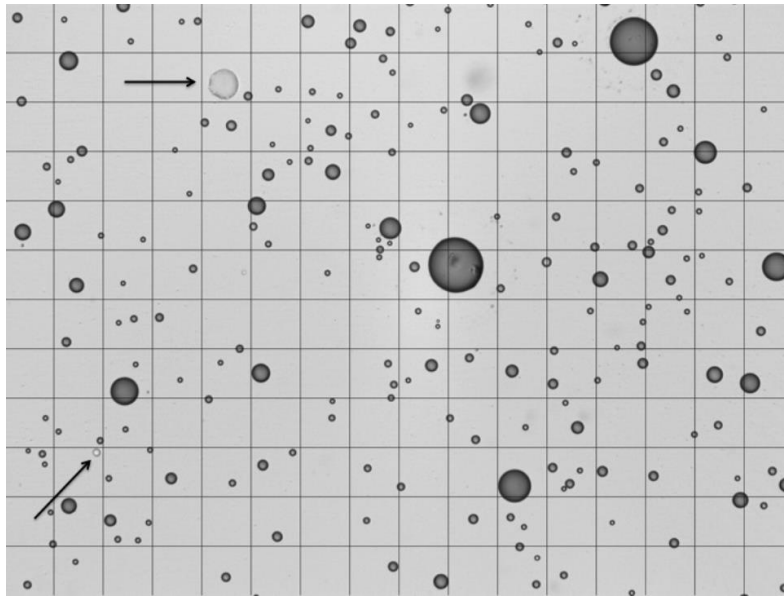


Figure 6: An image of a portion of a slide taken by the optical microscope. The grid spacing is 37 μm . 350 images are taken per slide. Two arrows point towards two droplets, which are flatter due to reduced surface tension, possibly due to containing organics, resulting in lighter coloring. Figure 4 from Jensen et al. (2020a).

The external impaction method developed by Jensen et al. (2020a) using the GNI is powerful in that it provides the benefits of a large sample volume useful for improved statistics for large SSA, a common issue with many sampling methods. In addition, it can distinguish between salt particles and non-salt particles. There are a few drawbacks to this method as well, including possible coalescence between the spherical cap droplets when they grow in the humid chamber and potential breakup of drops when they collide with the slide at the high speed of the aircraft. However, Jensen et al. (2020b) used a stochastic Monte-Carlo model for coalescence on the slide, finding that particle loss to coalescence was generally <5%, resulting in only small uncertainty. Additionally, Jensen et al. (2020b) found that the breakup of particles with $r_d > 11 \mu\text{m}$ does not occur frequently enough to change the concentration of smaller particles ($r_d < 11 \mu\text{m}$). The biggest drawback of the GNI is the reality that aircraft observation is expensive and infrequent, thereby resulting in a low frequency of sampling.

1.5 Study objectives

The primary goal of this project is to design and create a new, low-cost instrument that can sample SSA using an accessible platform. A secondary goal is to determine what environmental conditions influence SSA size and number concentration. To accomplish these objectives, a new instrument known as the miniature Giant Nucleus Impactor, or mini-GNI was designed and created. It is a low-cost instrument using Arduino technology, housed in a 3D-printed body.

A kite platform is used for sampling due to its relative simplicity and ease of access, similar to the reasoning inspiring Daniels (1989). The kite platform offers the opportunity to sample in the same location across seasons, times of day, environmental conditions, as well as to sample many altitudes simultaneously.

Chapter 2: Methodology

2.1 Instrument Design

2.1.1 Mini-GNI

The mini-GNI was designed to sample SSA onboard a kite platform using external impaction; the final design of the mini-GNI is shown in Figure 7. The mini-GNI houses its electronics in a 3D printed body consisting of three parts: a base, arm, and door. The 3D printed body was designed using Fusion 360 software. The base has a wing wrapped with a lightweight material, such as a plastic wrap, to orient the mini-GNI and the adhered polycarbonate slide in the direction of the wind. When the door opens, the arm extends from the mini-GNI via a spring exposing a polycarbonate slide to the SSA in the free atmosphere.

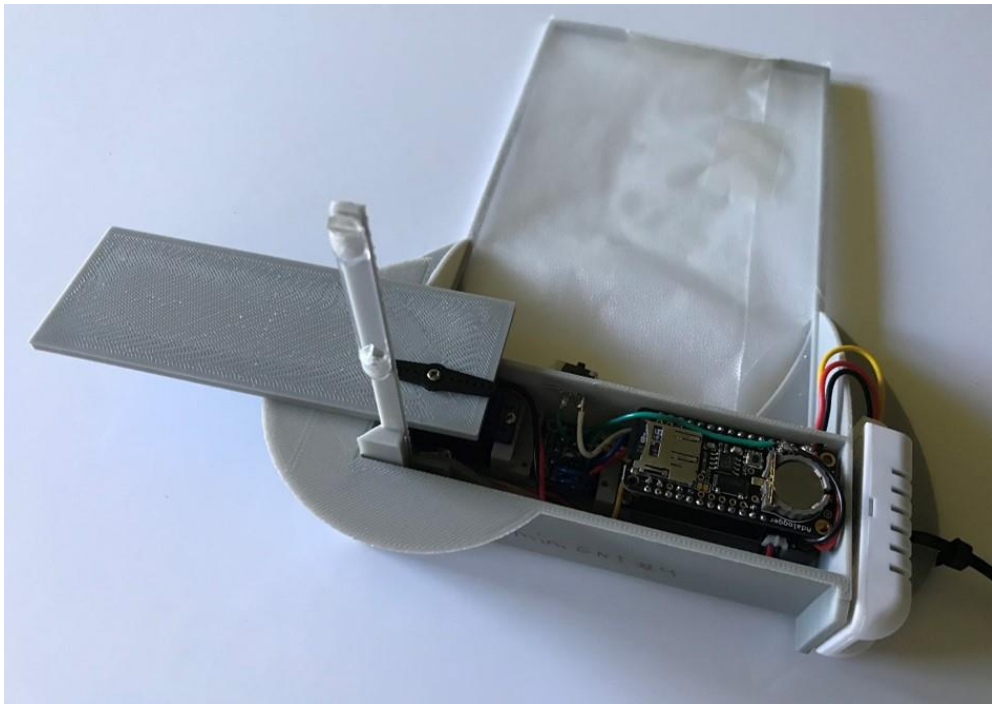


Figure 7: A photograph of the mini-GNI with its door open showing the exposed polycarbonate slide on the instrument's arm.

The mini-GNI operates using an Adafruit Feather M0 board and uses a variety of Adafruit sensors and microcontrollers. A complete description of the creation of the mini-GNI including 3D printed parts and electronics are given in Chapter 7: Appendix.

A brief overview of the sensors and microcontrollers that make up the mini-GNI are as follows. The Adafruit Feather M0 board has a RFM95 Long Range (LoRa) Radio module for communication to the ground while the instrument is in flight. The Adalogger FeatherWing with Real Time Clock (RTC) and micro SD card add-ons provides time keeping and data storage. A micro servo opens and closes the door, acting to extend and retract the arm and the attached polycarbonate slide. The MPL3115A2 sensor measures pressure with 1.5 Pa resolution, and the AM2302 sensor measures temperature with 0.5 °C uncertainty and RH within 2-5% (Adafruit 2020). The BNO055 Absolute Orientation sensor provides the orientation of the instrument in Euler angles relative to an initial position recorded when the instrument is powered on. A 3.7 V, 150 mAh lithium ion polymer battery powers the mini-GNI while a CR1220 3 V coin cell battery powers the RTC add-on.

A control station is used to communicate with the mini-GNI from the ground. The control station also uses a 3D printed body to house the electronics and an Adafruit Feather M0 board with RFM95 LoRa Radio for communication (Figure 8). The touchscreen is a TFT FeatherWing that displays information received by the mini-GNI and has touch screen buttons to open or close the door of the mini-GNI. The parts are detailed in Chapter 7: Appendix (Table A2). The control station is also powered by a 3.7 V, 350 mAh lithium ion polymer battery. Each mini-GNI has its own corresponding control station. Each pair communicates at different frequencies, all of which are around 900 MHz. The mini-GNIs send information back to the control stations approximately every 3 secs.



Figure 8: A photograph of the touchscreen control station used to communicate with the mini-GNI instrument from the ground while the mini-GNI is aerially deployed.

2.1.2 Anemometer

In addition to the mini-GNI, a second instrument was designed to measure wind speed at altitude: two custom anemometers were built to observe the wind profile at the sampling location. Similar to the mini-GNI, the custom anemometers have an Adafruit Feather M0 board with a RFM95 LoRa module, an Adalogger FeatherWing with RTC and micro SD card add-ons, and a MPL3115A2 sensor inside. They additionally contain a modified Noctua NF-A4x10 5V fan used to measure wind speed (Figure 9). The modified Noctua fans were calibrated in a wind tunnel prior to attachment to the 3D printed body by John Leeman of Leeman Geophysical LCC. Unfortunately additional calibrations after development were not possible, so potential calibration errors may be present and are not quantified.

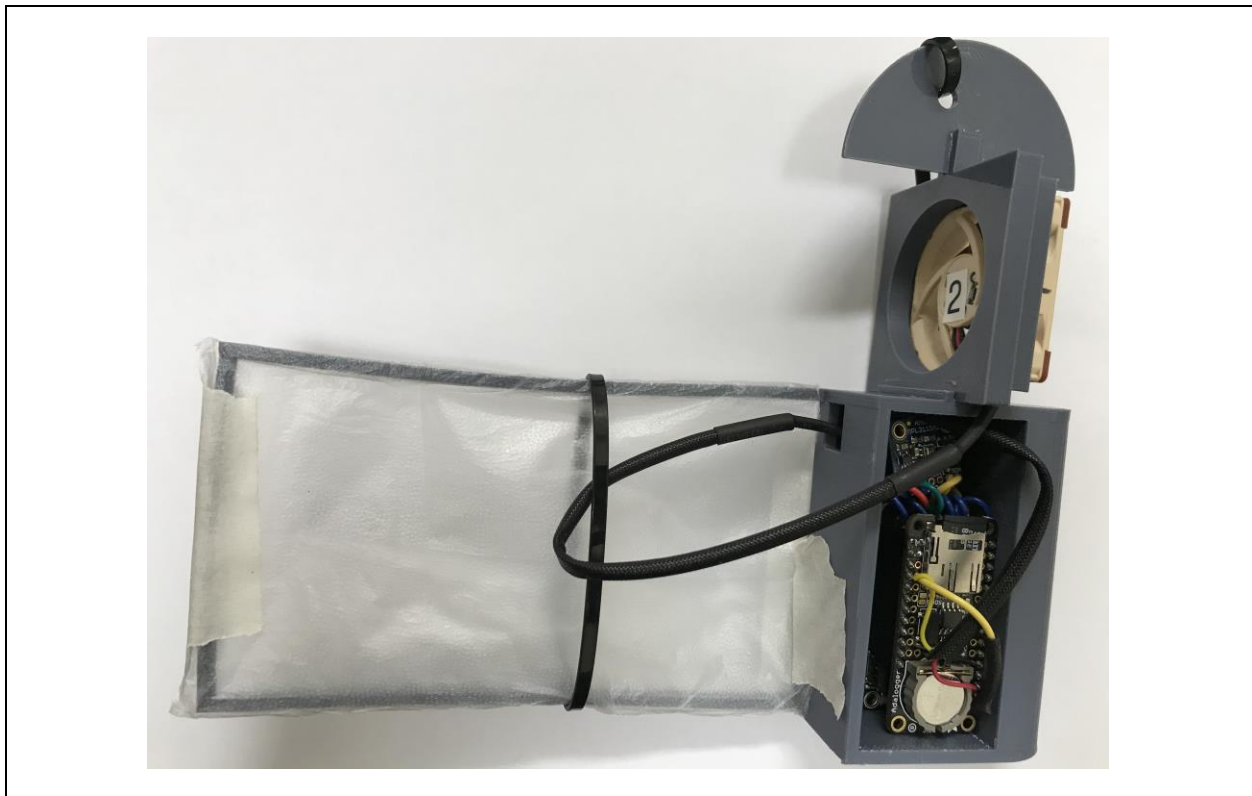
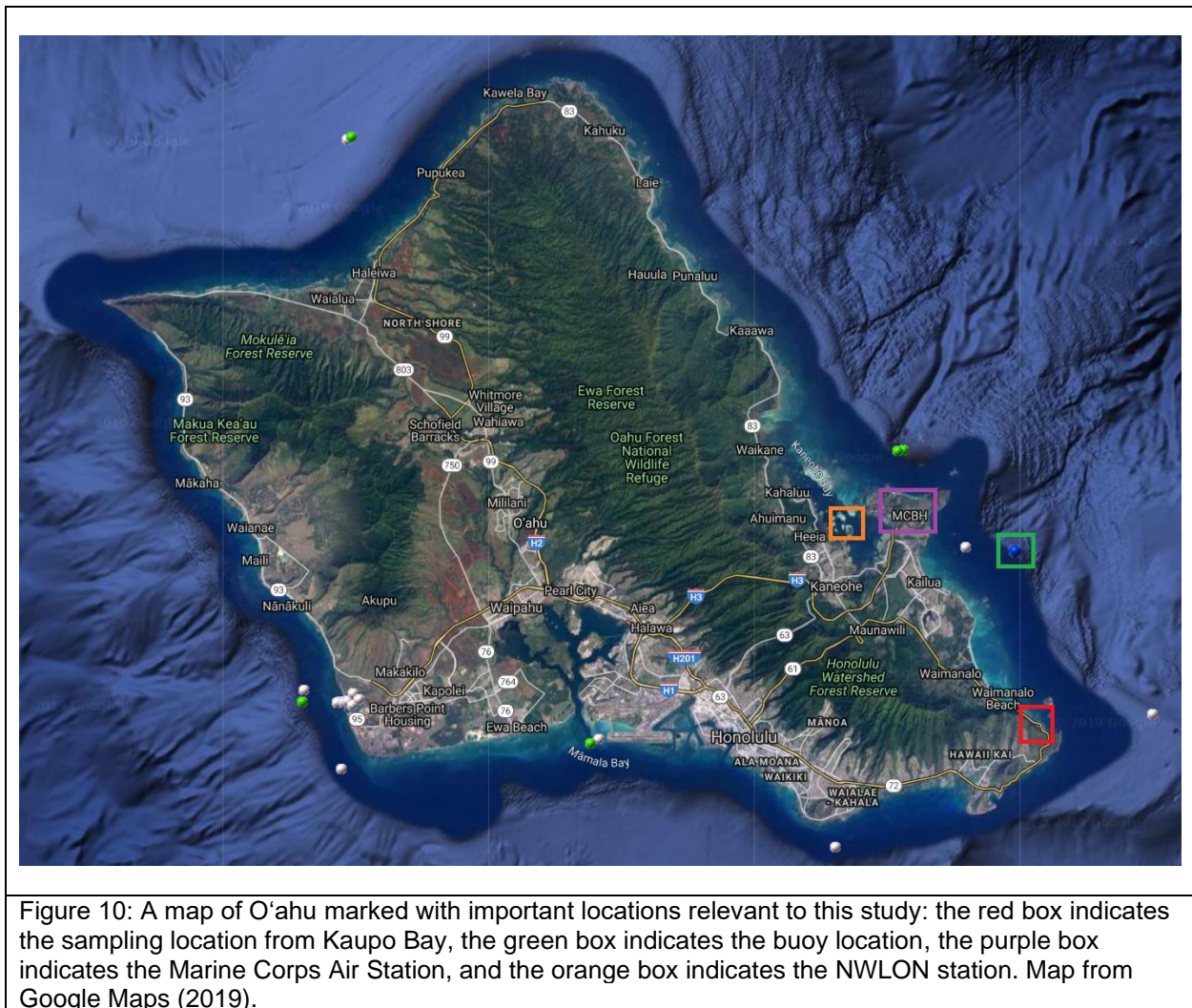


Figure 9: A photograph of the custom anemometer. The wing on the left orients the fan (offwhite color object at top) in the direction of the wind. The Adafruit FeatherWing electronics are visible inside the anemometer housing.

2.2 Kite Sampling and Environmental Data

A location called Kaupo Bay on the windward side of O'ahu was chosen as the sampling location due to its direct exposure to strong trade winds and its relative ease of access (red box in Figure 10). The SSA size distribution was observed from the coastline at Kaupo Bay at various times from December 2018 to September 2019. Wave data is obtained from a buoy off the windward coast of O'ahu (McManus 2014), historical wind data is obtained from the Marine Corps Air Station (National Weather Service 2019), and tide data is obtained from a National Water Level Observation Network (NWLON) station (CO-OPS 2020). The sampling, buoy, NWLON and weather station locations are displayed in Figure 10. Finally, bathymetry and topography data was accessed from the National Geophysical Data Center (NCEI 2020).



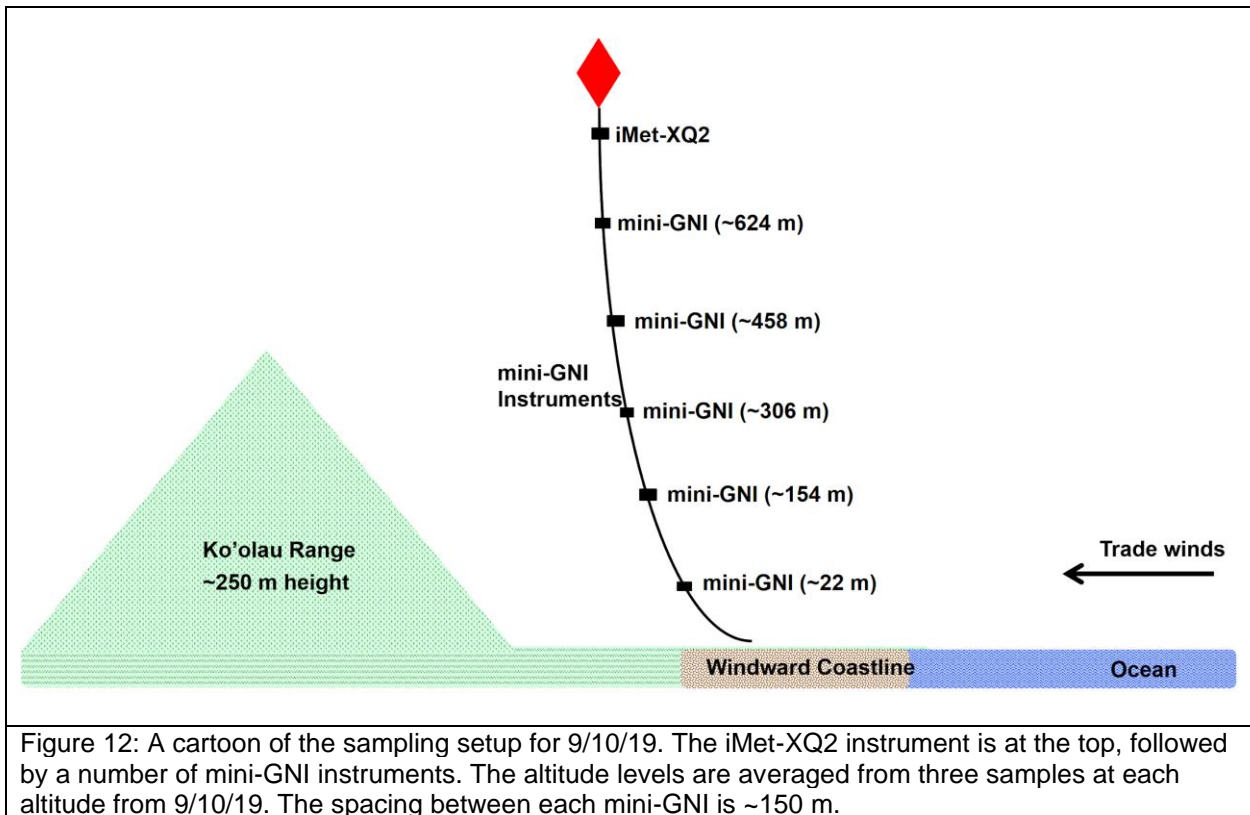
The mini-GNI is lofted into the atmospheric boundary layer on a kite platform. The mini-GNI instruments are attached to the kite string with a carabiner (Figure 11). The kite string has significant tension while the kite is flying, which keeps the carabiner in place. For kite string, we use 80 lb test braided fishing line. The line is deployed using an electric fishing reel with a line counter that displays the amount of line extended. For sampling, the instruments aloft need to be as stable as possible with a high string angle. To achieve this, a delta conyne kite is used; it is a combination of a box kite and a delta kite, known to be stable and easy to use with strong lift.



Figure 11: A photograph of a mini-GNI instrument attached with a carabiner to the kite string using a black zip tie. Notice that the door is closed until the instrument reaches the desired altitude, and an orange streamer is also attached for visibility.

On a typical sampling day, the kite is deployed to 25-50 m and once steady, the kite line is extended and instruments are attached serially along the kite string. An iMet-XQ2 instrument is always attached first to ensure that it is the highest instrument while a second iMet-XQ2 is left at the ground surface. The iMet-XQ2 instruments are purchased from Internet Systems Inc. and provide GPS information, pressure, humidity, and temperature measurements. Since these instruments keep GPS time, the iMet-XQ2 aloft is used to correct time errors in the RTC add-ons on the mini-GNIs. Meanwhile, the iMet-XQ2 left at ground level provides surface pressure which is used as a reference pressure to calculate the altitude of each mini-GNI.

Following the deployment of the iMet-XQ2, the mini-GNIs are attached, all with new polycarbonate slides. The mini-GNIs are attached to the kite string at various string length intervals, usually with between 50 to 200 m spacing depending on the sampling day; the spacing increases for sampling days with higher maximum altitude (Figure 12). Once the mini-GNIs are all lofted and at a stable altitude, the remote ground control stations are used to open the mini-GNI doors with the LoRa connection. Opening the door exposes the polycarbonate slides which are left exposed at altitude for a set duration, typically 10 mins. After exposure, the doors are closed, withdrawing the polycarbonate slide, and the kite is reeled in. The mini-GNI instruments are detached and collected one-by-one, and the slides are removed and placed into desiccant tubes. New slides are attached to the mini-GNI arms, and the process is repeated two additional times to obtain three samples for each altitude.



2.3 Microscope Analysis

The desiccant tubes are sent to the National Center for Atmospheric Research (NCAR) for analysis with the GNI microscope (Jensen 2020a). The microscope takes images of the humidified particles, and the software computes a raw count for dry radius size bins as was described in Chapter 3. The size

distribution is computed using Equation 1, which involves the sample volume and collision efficiency (CE) of SSA particles impacting the polycarbonate slide. The CE represents the fraction of particles that impact onto the slide instead of following the air stream around it. This impaction is dependent on each particle's inertia; larger particles have a higher CE than smaller particles. The CE can be estimated by considering the experiment as an air stream with aerosols impacting an infinitely long ribbon with finite width (Ranz and Wong 1952). The method employs the following sets of equations, where Equations 3-5 are used to break down Equation 2:

$$CE = \frac{S_2 - S_1}{S_2 \exp(S_1 a) - S_1 \exp(S_2 a)} \quad (\text{Eq. 2}),$$

$$S_{12} = -\frac{1}{4\psi} \pm \sqrt{\left(\frac{1}{4\psi}\right)^2 + \frac{1}{2\psi}} \quad (\text{Eq. 3}),$$

$$a = \frac{1}{b} \tan^{-1} \left(\frac{4\psi b}{8\psi - 1} \right) \quad (\text{Eq. 4}),$$

$$b = \sqrt{\frac{1}{\psi} - \left(\frac{1}{4\psi}\right)^2} \quad (\text{Eq. 5}),$$

where S_1 and S_2 are the plus and minus versions of Equation 3, and ψ is the ratio of the force required to stop a moving particle to the fluid resistance (Ranz and Wong 1952). The variable ψ is defined as

$$\psi = \frac{C\rho_p v_0 D_p^2}{18\mu D_c} \quad (\text{Eq. 6}),$$

where C is the Cunningham correction factor, ρ_p is the particle density, v_0 is the air stream speed, D_p is the particle diameter, μ is the dynamic viscosity of air, and D_c is the width of the collector (Ranz and Wong 1952).

The collision efficiency calculation from Ranz and Wong (1952) is illustrated in Figure 13 where it becomes clear that CE increases as particle inertia increases through increasing dry radius particle size or wind speed.

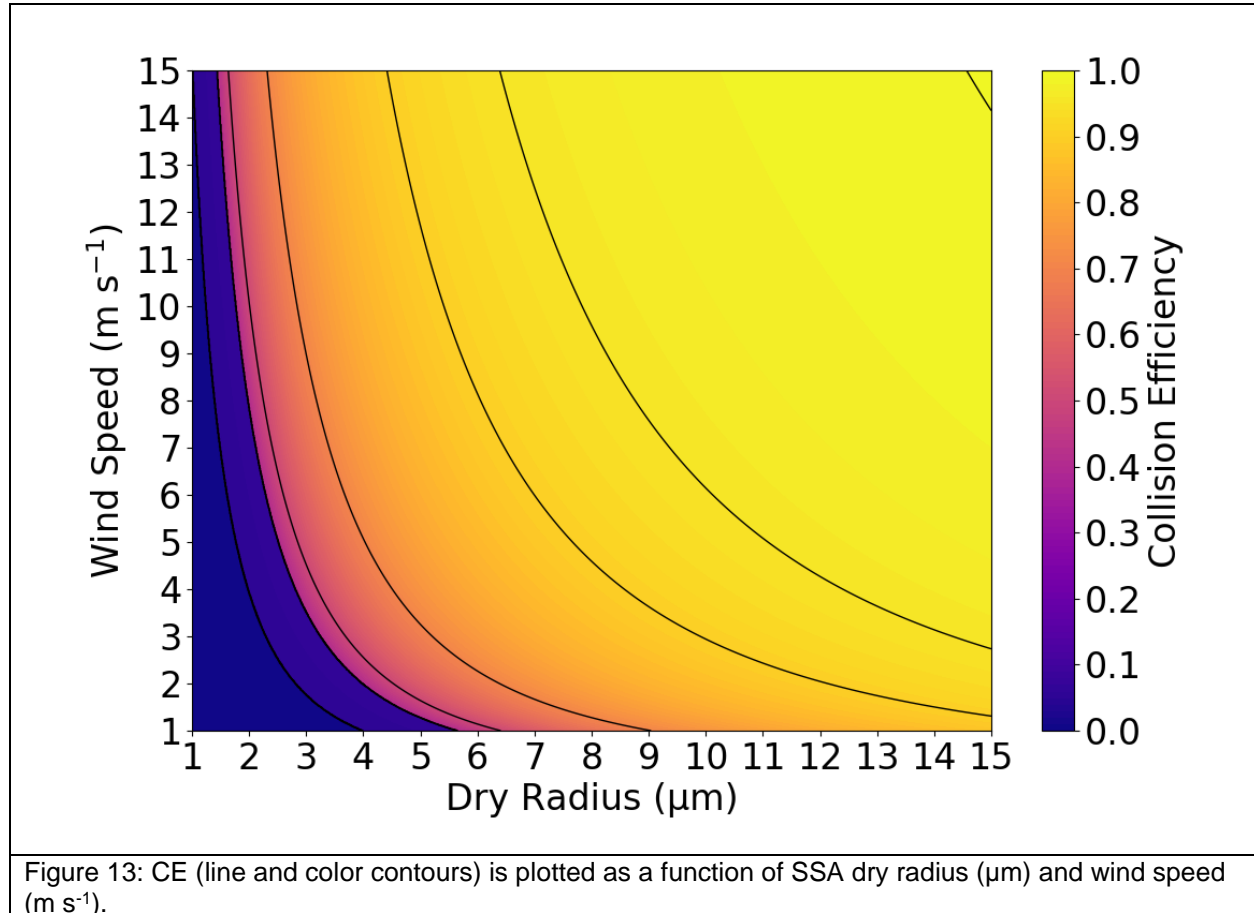
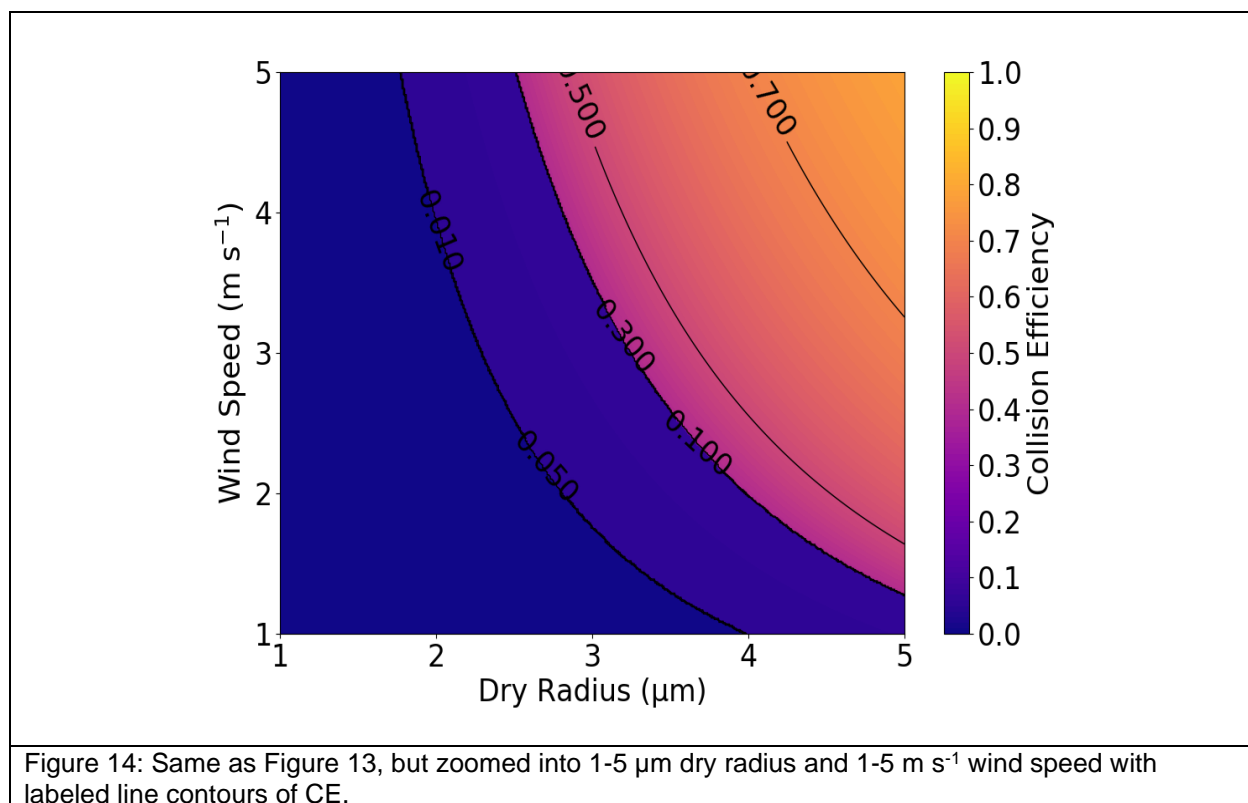


Figure 14 is a zoomed version of Figure 13 with labeled contour lines to show the sharp gradient in CE at low values. For example, when holding the wind speed at 3 m s^{-1} , increasing the particle size from 3.2 to $3.3 \mu\text{m}$ causes a jump in CE from 6% to 41% . This jump in CE is a discontinuous jump as a result of the denominator of the arctan function as the variable ψ increases towards 0.25 . The value inside the arctan function approaches negative infinity and then jumps to the limit of positive infinity. The arctan function discontinuously therefore jumps from -1.57 to $+1.57$, resulting in the discontinuous jump in CE. Such a discontinuity is not physical, so steps detailed in Chapter 3 are taken to avoid it.



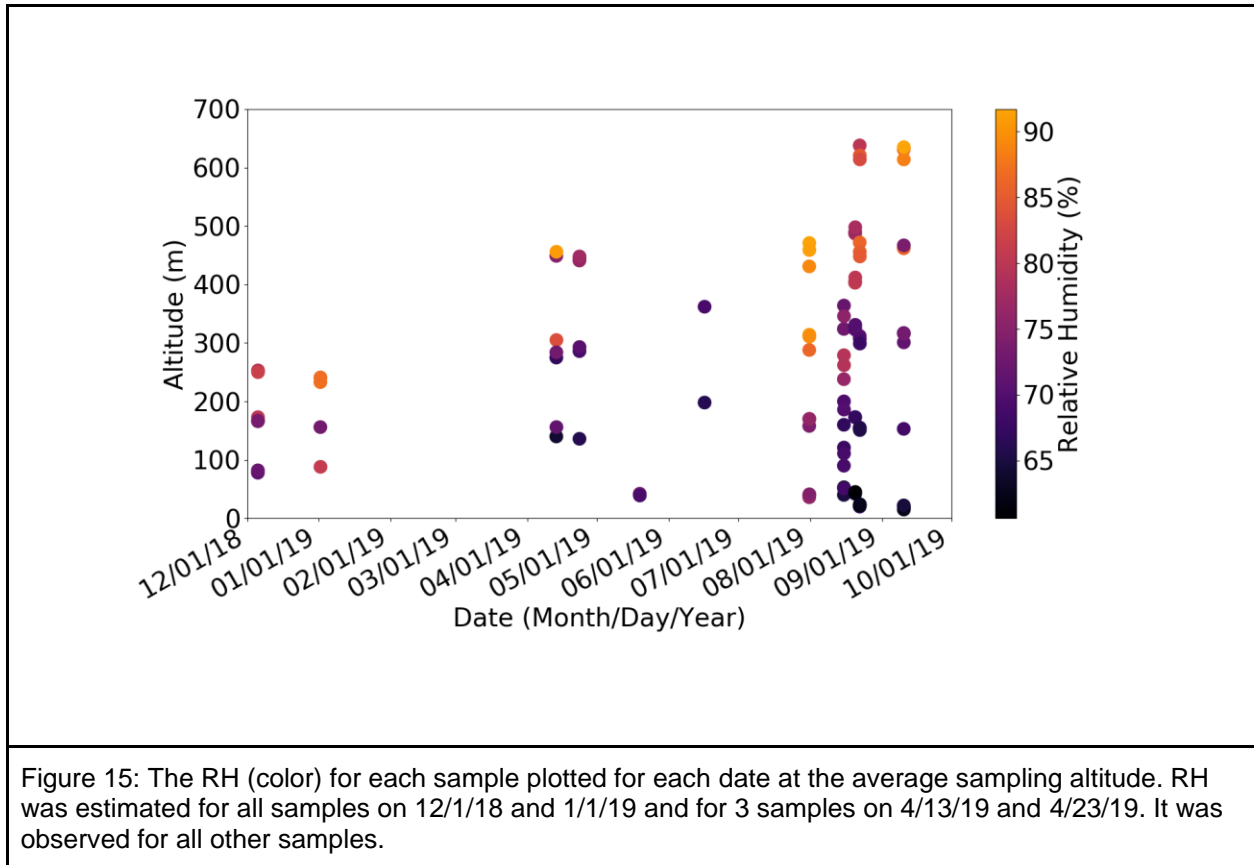
2.4 Environmental Variables

Due to the importance of CE in determining the number concentration, it is necessary to measure pressure, temperature, humidity, and wind speed aloft at each instrument during the sampling period. The pressure, temperature, and humidity are measured by the various Adafruit sensors on the mini-GNI. Steps to obtain estimates for the other variables are outlined as follows.

2.4.1 Relative Humidity

While RH is currently measured by the mini-GNI, this was not the case for 14 of the 95 samples collected between December 2018 and January 2019 since initially, not every mini-GNI had a humidity sensor. For these samples, the humidity aloft was estimated by measuring humidity and temperature at the surface, calculating the water vapor pressure and assuming that the boundary layer was well-mixed. The vapor pressure at each instrument deployed from 90 - 250 m was assumed to be the same as at the surface. Therefore, given the temperature at each instrument, the humidity was calculated using the surface value of vapor pressure. In Figure 15, we find that our estimates of RH for the 12/1/18 and 1/1/19

samples fit within the range of observed RH across all sample dates implying that the RH estimates are reasonable.



2.4.2 Wind Speed Aloft

Wind speed aloft is especially important for observation of SSA because both sample volume and CE depend on it. However, the custom anemometer was not available throughout much of the project for simultaneous in-situ measurement of wind speed aloft. Wind speed aloft was instead estimated using the surface wind speed and known wind relationships with height. Surface wind measurements of speed and direction were measured using a tripod-mounted Kestrel and averaged over each sampling period. A Kestrel is a small hand-held instrument that measures wind speed with a propeller anemometer at accuracies of 1.04-1.66% (Kestrel 2015). The Kestrel sits approximately 7 ft (~2 m) above the ground and the land declines towards the beach such that the Kestrel sits nearly 20 ft (~6 m) above the sea. These near-surface measurements of wind speed are used to estimate the wind speed (u) aloft at an altitude z with the wind profile power law (Arya 2001),

$$\frac{u}{u_r} = \left(\frac{z}{z_r} \right)^m \quad (\text{Eq. 7}),$$

where u_r is the wind speed at the reference height, z_r , commonly defined as 10 m. The exponent m is 1/7 for smooth surfaces and increases with increasing stability or roughness. The power law is used because it fits observed wind speed profiles in the lower planetary boundary layer (Arya 2001). It is a good predictor of wind speed profiles over simple, or flatter, terrain (Peterson and Hennessey Jr. 1977). Given that the terrain of the sampling location is relatively flat and simple, the power law was chosen to estimate wind speed aloft.

Though the power law provides reasonable empirical fit to observations, the log law works better for complex terrain and also has a sounder theoretical basis (Arya 2001). The log law is given by

$$\frac{u}{u_r} = \frac{\ln(z/z_0)}{\ln(z_r/z_0)} \quad (\text{Eq. 8}),$$

where u is the mean flow velocity at height z above the ground, z_0 is the roughness length, and u_r is the wind speed at some reference altitude, z_r . The uncertainty introduced by estimating wind is examined in a sensitivity study discussed in Section 4.4: Sensitivity Study.

2.4.3 Other Variables

Altitude and time also require estimation or post-sampling processing. The altitude of the mini-GNI is calculated with pressure observed from the included barometer. Each sampling day, all barometers are calibrated to the surface pressure measurement from the iMet-XQ2 instrument left at the surface averaged over the sampling period. The time of each mini-GNI is given by its Real Time Clock (RTC) add-on, which tends to drift over time. This is corrected by flying an iMet-XQ2 instrument on the kite string at the top, above all the mini-GNI instruments. The iMet-XQ2 receives GPS data, so it records time accurately. Post sampling, the altitude time series of the iMet-XQ2 is compared with those of each mini-GNI. Each instrument on the kite string experiences the same dips and rises as the kite fluctuates in altitude, so the time series of each mini-GNI can be lined up with that of the iMet-XQ2 and corrected in post processing.

Chapter 3: Results

A total of 95 valid samples were collected and analyzed. Results indicate that the mini-GNI instruments deployed on the kite platform are capable of reliably measuring the SSA size distribution. This conclusion is made by comparing new size distributions collected with the mini-GNI to those obtained during the VOCALS-REx field campaign with the GNI (Figure 16).

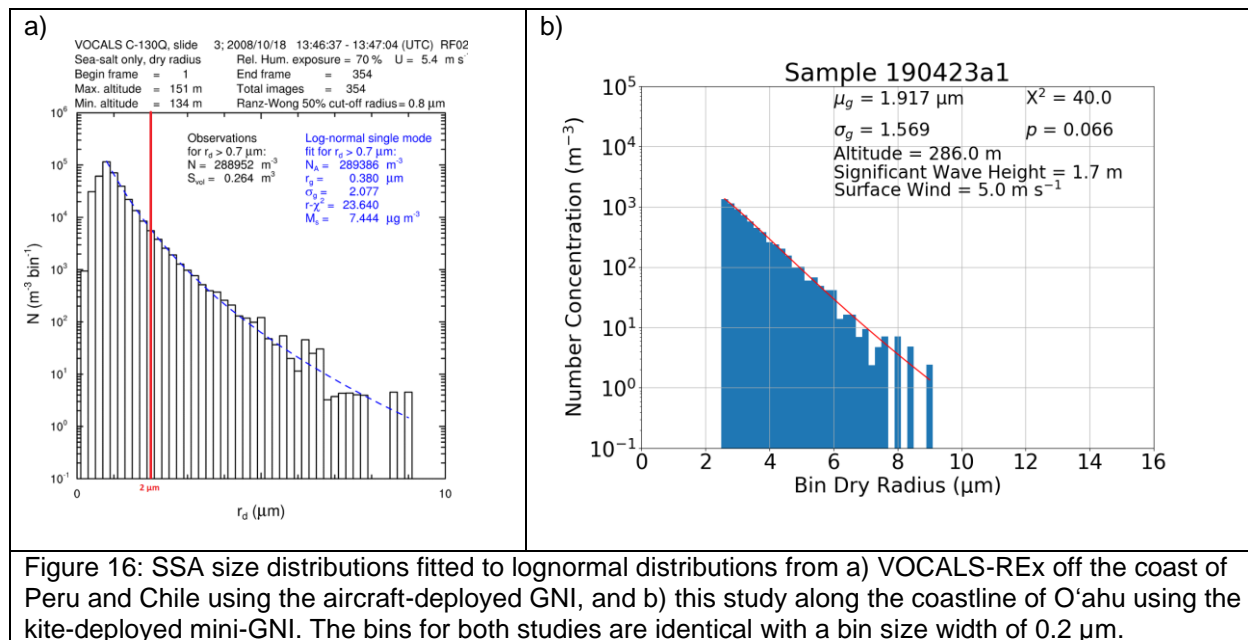


Figure 16: SSA size distributions fitted to lognormal distributions from a) VOCALS-REx off the coast of Peru and Chile using the aircraft-deployed GNI, and b) this study along the coastline of O’ahu using the kite-deployed mini-GNI. The bins for both studies are identical with a bin size width of 0.2 μm.

Figure 16b confirms that the kite-based platform is capable of observing the SSA size distribution. The mini-GNI cannot capture SSA of small size ($r_d < 2 \mu\text{m}$) due to the CE falling to 0 in those size ranges. However, comparing Figure 16a and b above 2 μm, the shape of the size distributions are similar despite the many differences involved in sampling, including location, date, altitude, platform, instrument and more (Figure 16). This is important for ensuring our results are trustworthy because while differences in the sea salt number and size are expected based on various environmental conditions that will be discussed, the general shape of the size distribution should be consistent with prior results and known relationships.

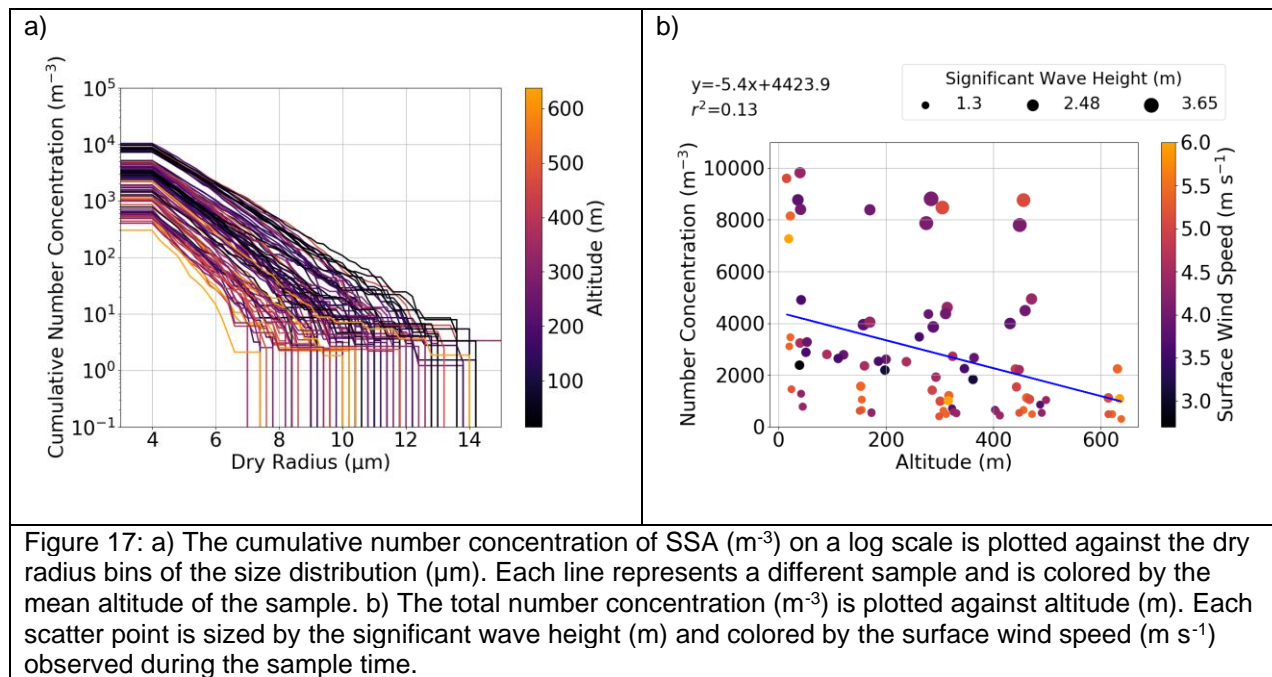
The 95 samples collected by the mini-GNI were obtained on 11 different sample days, and as such, samples were collected under different wind and RH conditions resulting in different CEs. To limit uncertainty, data from bins where CE < 40% was removed. The threshold of 40% was chosen to avoid

the discontinuous jump in CE, described in Section 2.3, which results in CE jumping from slightly above 40% to below 10%. Because each sample has a different CE, the calculation of total concentration is affected by the lower limit or cutoff size bin. To eliminate this potential bias when calculating cumulative concentration and total concentration, calculations always begin with the 3.9-4.1 μm bin for every sample. This 3.9 μm cutoff was chosen because all samples have greater than 40% CE above 3.9 μm .

In the following sections, the environmental conditions that influence SSA concentration are examined. First are altitude and wind speed, the variables that Woodcock examined in his studies, and then are wave height and wind history, two additional variables that were investigated.

3.1 Altitude

Based on results from prior studies, it was hypothesized that larger sea-salt aerosols would be more prevalent in the lower portion of the boundary layer (Woodcock 1953, Blanchard et al. 1984, and Daniels 1989).



Results from the present study are overall consistent with the findings from Woodcock (Figure 2), Blanchard et al. (Figure 3), and Daniels (Figure 4) with the caveat that SSA is fairly well mixed in mini-GNI SSA samples up to about 450 m. Large amounts of SSA were even found in some samples at 450 m.

However, samples with altitude higher than 450 m generally have very low concentration; the overall r^2 value of 0.13 for the correlation between SSA concentration and altitude indicates a relatively weak but robust relationship of decreasing SSA with altitude (Figure 17).

The correlation of SSA with altitude is likely weak because this result combines many sampling days which experience largely different environmental conditions, so the individual sampling days are also examined. Figure 18 shows that SSA is well-mixed with altitude for many sample days. However, SSA also decreases with altitude for some sample days: 7/31/19 (Figure 18e), 8/22/19 (Figure 18h), and 9/10/19 (Figure 18i). Surprisingly, the SSA concentration even seems to increase slightly with altitude on some sample days: 4/13/19 (Figure 18c) and 4/23/19 (Figure 18d). In summary, there is no consistent pattern of SSA concentration with altitude on individual sampling days, and only a weak overall relationship in the altitude range observed in this study.

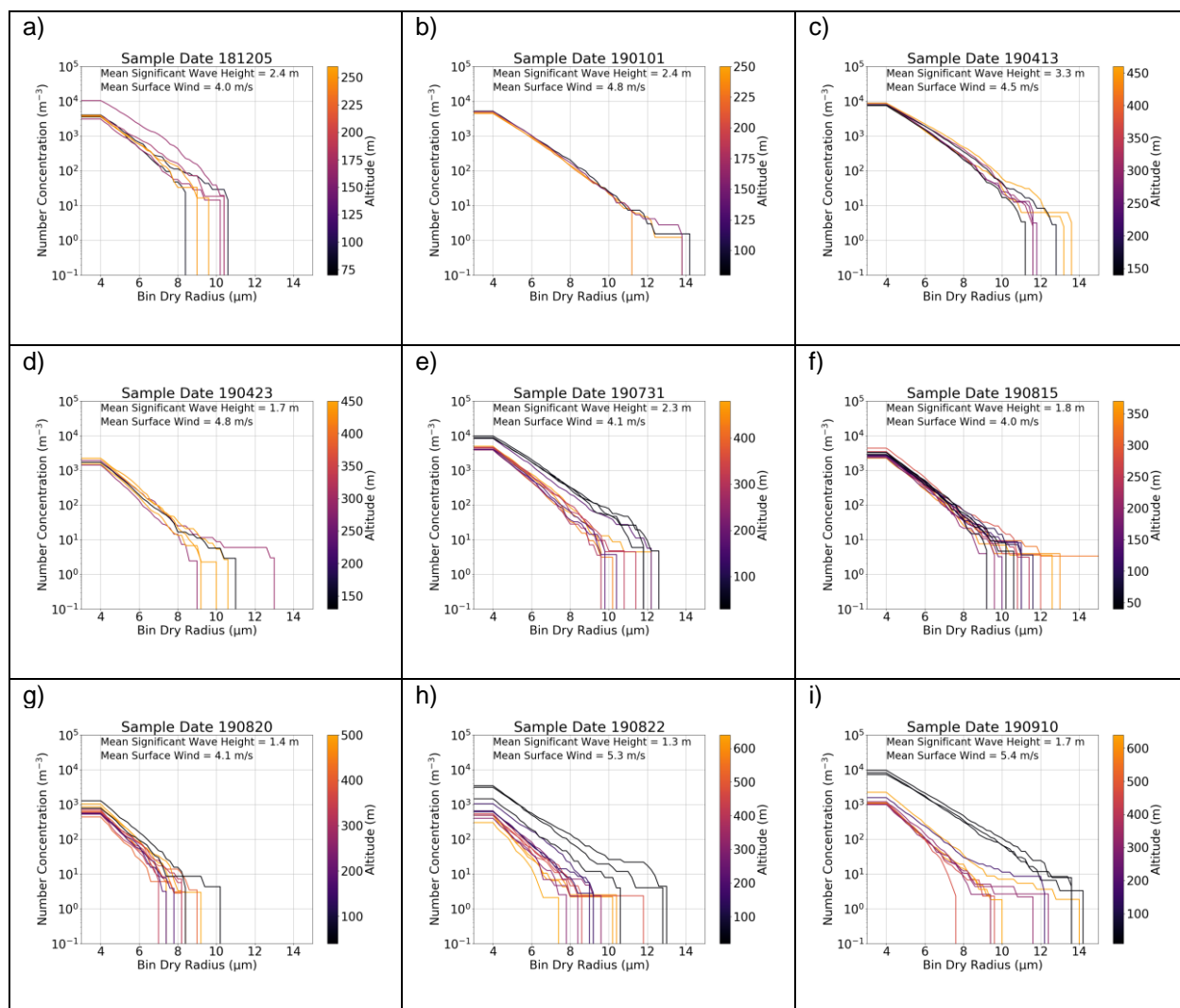
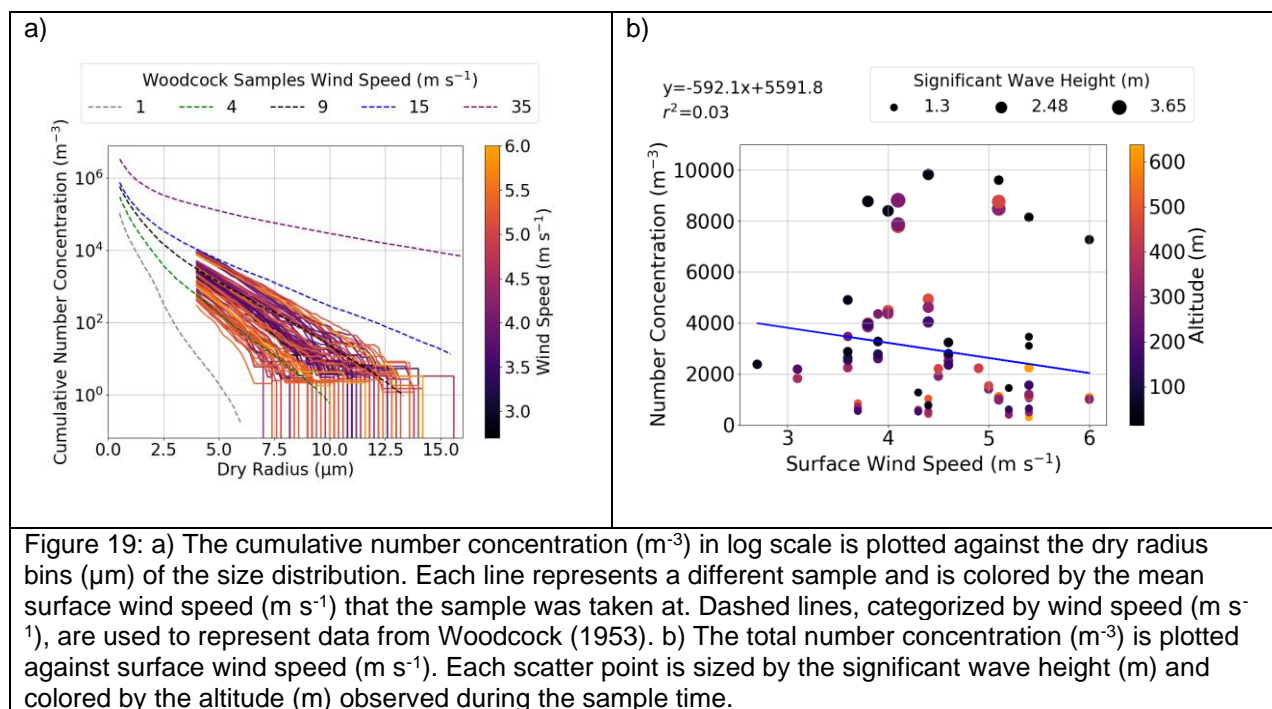


Figure 18: For each sampling day with >2 samples, the cumulative number concentration (m^{-3}) is plotted against dry radius bins (μm) of the size distribution. Each line represents a different sample and is colored by the mean altitude during sample collection. The sampling days with > 2 samples are a) 12/5/18, b) 1/1/19, c) 4/13/19, d) 4/23/19, e) 7/31/19, f) 8/15/19, g) 8/20/19, h) 8/22/19, and i) 9/10/19.

3.2 Wind Speed

Next, the relationship between SSA concentration and wind speed is investigated. Based on the results of Woodcock (1953), it was hypothesized that higher wind speeds would be associated with larger and more numerous SSA. Results from the mini-GNI are directly compared to Woodcock (1953) and are approximately constrained by Woodcock's 4 m s^{-1} and 15 m s^{-1} sample, though the relationship is not robust (Figure 19a). Observations from Woodcock (1953) explore a wider range of wind speeds and altitude than were observed in the present study with the mini-GNI, which ranged from only $\sim 3\text{-}6 \text{ m s}^{-1}$. Some of the low wind ($\sim 4 \text{ m s}^{-1}$) observations contained more SSA than Woodcock's 9 m s^{-1} sample, and

some of the high wind ($\sim 5.5 \text{ m s}^{-1}$) observations contained less SSA than Woodcock's 4 m s^{-1} sample. While some of this variation can be explained by the different sample altitudes, there are even low altitude ($\sim 100 \text{ m}$) samples with relatively high wind speed ($\sim 5.5 \text{ m s}^{-1}$) that have low SSA concentration (Figure 19b). To explore this more explicitly, a plot of number concentration and surface wind speed shows a near zero r^2 value suggesting no relationship in the present study between SSA and instantaneous wind (Figure 19b). These results suggest that SSA observed by the mini-GNI along O'ahu's coastline were influenced by factors other than wind speed and have a more complicated explanation than the results from Woodcock (1953).

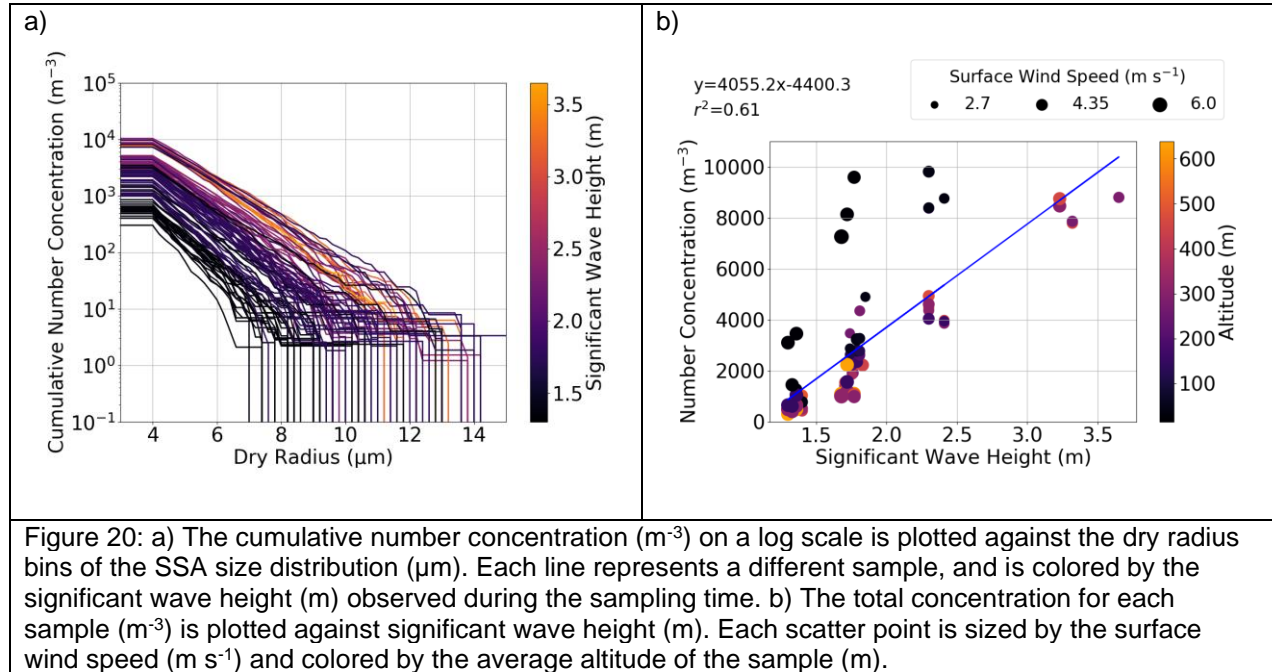


3.3 Wave Height

Next, wave height was examined; it was hypothesized that there would be a positive correlation between SSA concentration and significant wave height, defined as the mean wave height of the highest third of waves, because as described in Chapter 1, wave breaking is the primary source of SSA in the atmosphere. In Figure 18, results show that different sampling days have different amounts of SSA. Of particular note are the sampling days 4/13/19 (Figure 18c) and 4/23/19 (Figure 18d), which had similar wind speed (4.5 vs 4.8 m s^{-1}), but 4/23/19 observed more SSA. Of the environmental variables analyzed,

the biggest difference between the two sampling days was wave height. The buoy observed a significant wave height on 4/23/19 (3.3 m) that was nearly double the wave height on 4/13/19 (1.7 m).

Again, all samples are plotted together, but this time sorted by significant wave height (Figure 20). A strong positive correlation ($r^2 = 0.61$) between total SSA concentration and wave height was found, with higher wave heights resulting in more SSA in the atmosphere.



3.4 Wind History

While no strong relationships were seen in Sections 3.1 and 3.2 between SSA concentration and altitude nor instantaneous wind, Section 3.3 established a strong relationship between SSA concentration and significant wave height. Because waves are generated by a fetch, or a long term period of strong and directionally consistent winds over an area of water, wind history was investigated to provide additional insight.

Only instantaneous wind was observed with the Kestrel, so historical wind measurements are obtained from the Kaneohe Marine Corps Air Station (National Weather Service 2019), a high quality windward site near the sample location (orange box in Figure 10). Wind history is calculated as the average observed wind from the Kaneohe Marine Corps Air Station weather station over a particular

period of time prior to the time of sampling. The correlations of total SSA concentration with instantaneous wind and 12, 24, and 48 hour wind history are shown in Figure 21. A positive correlation was found between SSA concentration and wind history. The r^2 value increases from 0.03 with instantaneous wind to 0.27, 0.19, and 0.24 for 12, 24, and 48 hr wind histories respectively. These results suggest that a longer wind history is more strongly related to SSA number concentration, especially over the last day or two before sampling.

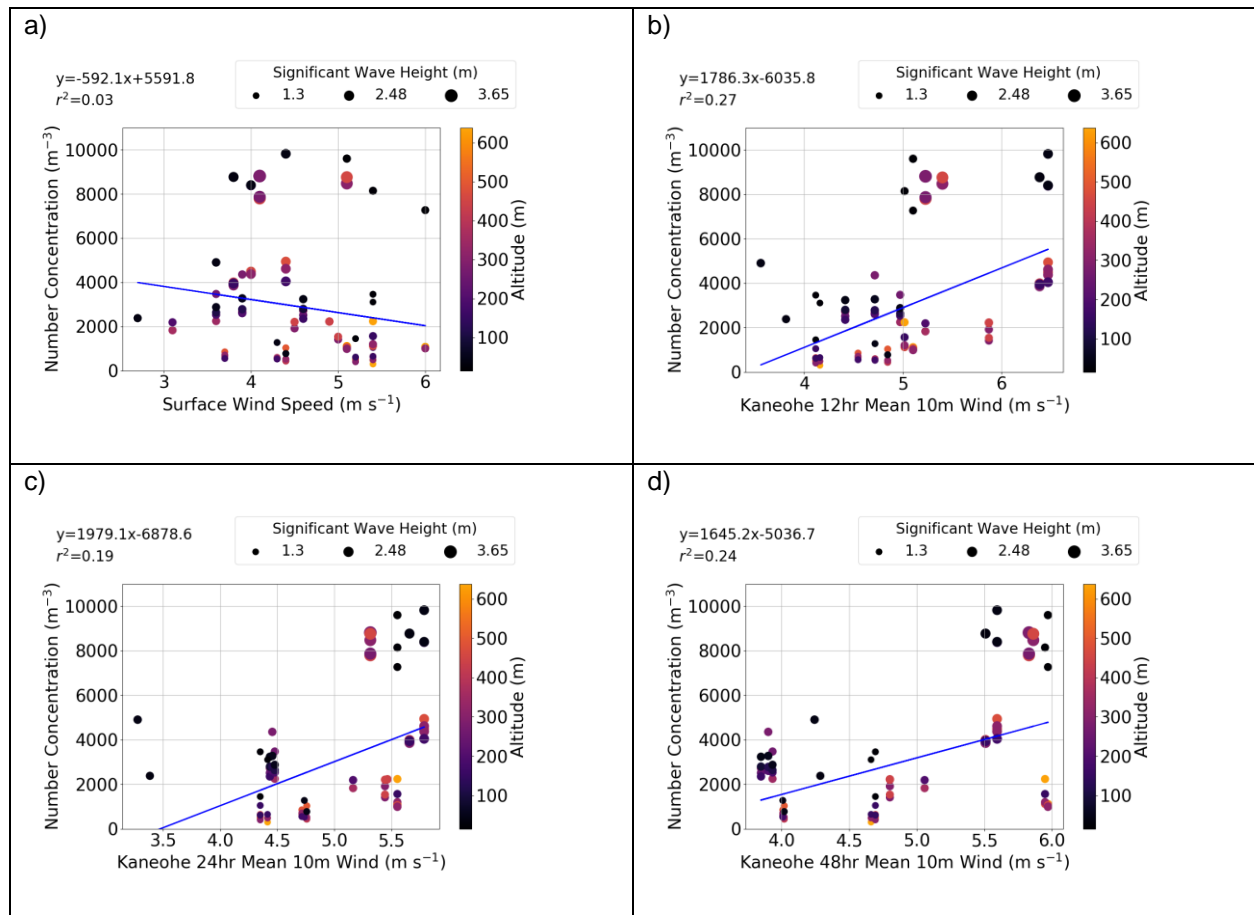


Figure 21: Total SSA number concentration (m^{-3}) is plotted against a) Instantaneous surface wind speed (m s^{-1}), b) 12-hour mean wind prior to sampling (all m s^{-1}), c) 24-hour mean wind prior to sampling, d) 48-hour mean wind prior to sampling. Scatter points are sized by the wave height (m) and colored by the average altitude (m) at which the sample was collected.

Chapter 4: Discussion and Conclusions

4.1 Local Production of SSA

In Chapter 3, the correlations between SSA concentration and altitude, instantaneous surface wind speed, significant wave height, and wind history were examined. In Section 3.1, a weak correlation was found between SSA concentration and altitude. SSA in the mini-GNI samples were generally well-mixed up to 450 m, and on some sampling days, more SSA was found at higher altitudes. However, on sampling days with high altitude (> 600 m) samples, there was a clear divide with low altitude samples (< 600 m) having more SSA than high altitude samples. A possible explanation for the well-mixed nature of SSA up to 450 m could be that SSA are lofted by orographic lift due to the proximity of the Ko'olau mountain range near the coast of O'ahu and near to the sampling location. Note that this result is not directly comparable to the Woodcock (1953) study because his samples were generally from higher altitudes, even up to 2000 m. The altitude range of the mini-GNI results are more comparable to the Blanchard et al. (1984) study, which observed samples below 30 m (Figure 3), finding that SSA concentration decreases sharply with height from 19.5-30 m in an average SSA concentration vertical profile. The present study observed six samples (leftmost points in Figure 17) between 15-24 m, finding a range of total number concentration between 1,452-9,601 m^{-3} , while the range of total number concentration of all 95 observed samples was between 301-10,384 m^{-3} . Additionally, 10 samples were observed between 36-53 m, finding a range of total number concentration between 777-9,822 m^{-3} . The present study therefore does not observe the same sharp decrease in SSA concentration at low altitude as Blanchard et al. (1984).

In Section 3.2, no correlation was found between SSA concentration and instantaneous surface wind speed. This finding is contrary not only to Woodcock's observations, but also to many numerical models for weather and climate that parameterize SSA production with wind speed. SSA production is typically parameterized in models using 10 m wind because strong winds cause waves to break and form whitecaps (Lewis and Schwartz 2004).

These contradictions with prior studies and numerical model parameterizations can be explained by the sampling location along the coast next to the surf zone. Woodcock (1953) and Blanchard et al. (1984)

observed primarily offshore, and model parameterizations are designed to represent SSA over the open ocean. This difference between the coastal zone and open ocean is crucial since SSA are produced by wave breaking. Over the open ocean, waves break under high wind speed conditions and through interaction of wave swell and winds. Meanwhile, in the surf zone, waves break more frequently, primarily due to their interaction with land as the ocean depth decreases. It was therefore hypothesized that the SSA observed in the mini-GNI observations are generated locally by waves breaking against the coastline of O'ahu. If SSA are generated locally by wave interaction with land, it is reasonable to find no relationship between SSA and instantaneous wind speed at the time of sampling. Instead, a positive correlation between SSA and variables that are related to wave breaking along the coast would be expected. Indeed, in Sections 3.3 and 3.4, positive correlations were found between SSA concentration and significant wave height and wind history. Given that SSA production is tied to wave breaking, it is reasonable that larger waves produce more and larger SSA due to more energetic wave breaking.

Meanwhile, the correlation between SSA concentration and wind history can be explained by the fact that waves are generated by a fetch, a long term period of strong and directionally consistent winds over an area of water. Given that the mini-GNI samples are always obtained on days with moderate to strong trade winds due to the limitations imposed by a kite-platform, it can be assumed that the waves breaking along the windward coast of O'ahu belong to a trade wind fetch. This assumption is given some credence by using HySPLIT trajectories to view the path of wind approaching O'ahu's coastline. The HySPLIT archive trajectories (Figure 22) were created using the online HySPLIT Trajectory Model on the Air Resources Laboratory (ARL) website (Stein et al. 2015 and Rolph et al. 2017). The air parcel backward trajectories from various sampling altitudes generally follow a straight line for 60 hrs, indicating a long fetch from an easterly or northeasterly direction as is expected on trade wind days. The only exception is the 12/5/18 sampling day (Figure 22a).

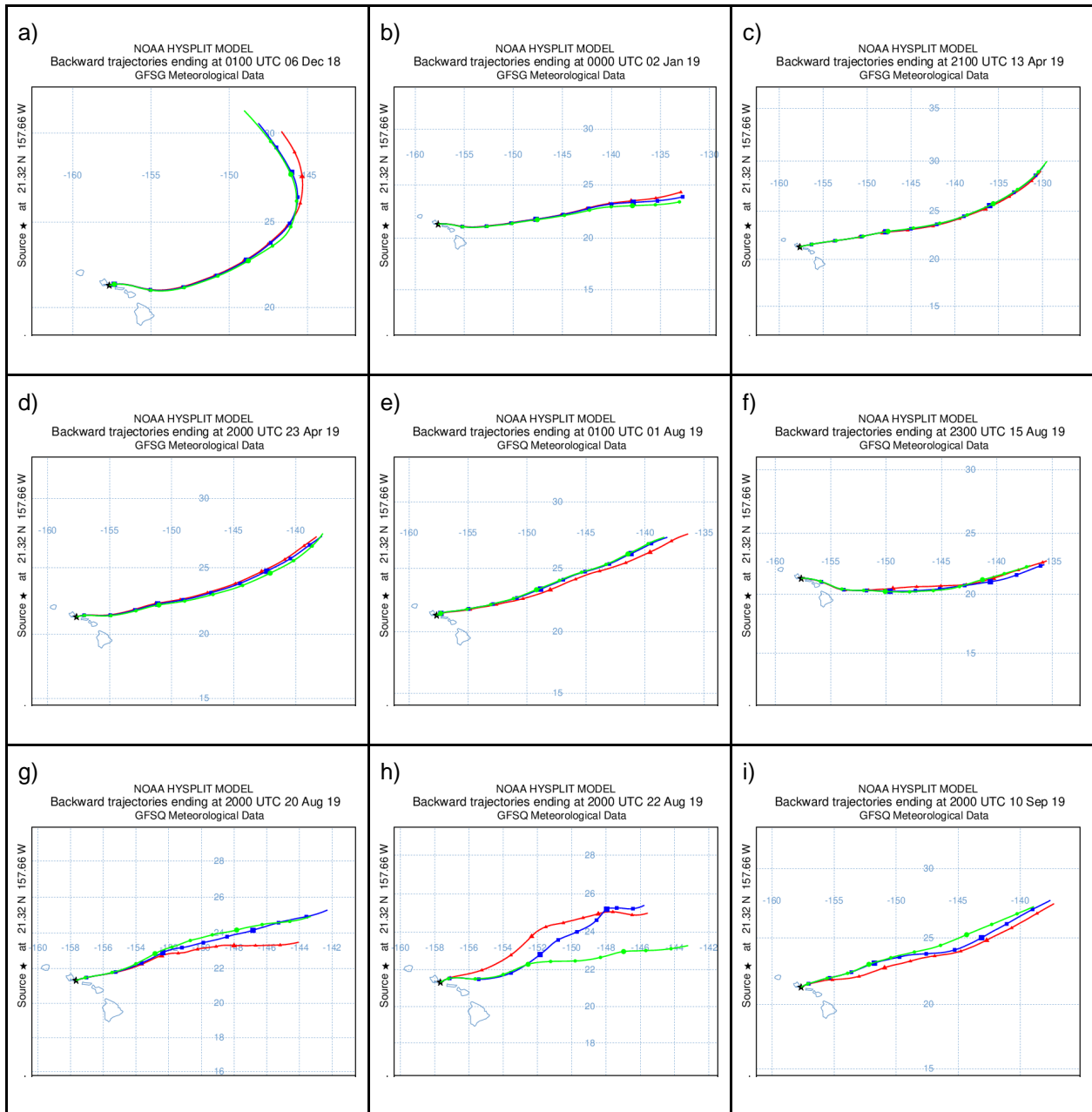


Figure 22: HySPLIT 60-hour back trajectories for sampling days a) 12/5/18, b) 1/1/19, c) 4/13/19, d) 4/23/19, e) 7/31/19, f) 8/15/19, g) 8/20/19, h) 8/22/19, i) 9/10/19. The green, blue, and red colors represent low, medium, and high altitude respectively, ranging from near-surface (~25 meters) to ~750 meters. Each point on the trajectory line marks a 6 hour interval.

Furthermore, if wave breaking on sample days is generated by a trade wind fetch, it can also be assumed that the wind history at Kaneohe Marine Corps Air Station is representative of the strength of trade winds in the Hawaiian region. This confirms a physical connection for the correlation found in Section 3.4; stronger trade winds lead to a stronger fetch, bringing stronger and larger waves to the

windward coast of O'ahu which generate more and larger SSA. This finding, along with the zero correlation found between SSA concentration and instantaneous wind speed, is evidence that locally generated SSA are observed by the mini-GNI.

The residence time of SSA can be considered to further support this argument. The residence time due to dry deposition for SSA of various r_{80} is given by Lewis and Schwartz (2004) in Figure 23. The variable r_{80} is the radius in equilibrium at 80% RH and is approximately twice the dry radius (Lewis and Schwartz 2004). The smallest particles observed in this study have $r_d \sim 2 \mu\text{m}$, or $r_{80} \sim 4 \mu\text{m}$, and the largest particles have $r_d \sim 10\text{-}15 \mu\text{m}$, or $r_{80} \sim 20\text{-}30 \mu\text{m}$. The SSA observed therefore have a dry deposition residence time between 5 mins to just above 10 hrs. Porter et al. (2003) showed that sea salt rises rapidly after being produced. Therefore, all but the smallest SSA observed ($r_d \sim 2 \mu\text{m}$) are most likely generated by local mechanisms.

$r_{80}/\mu\text{m}^a$	1	2	5	10	15	20	25
Dry deposition velocity, $v_d/(\text{cm s}^{-1})^b$	0.05	0.25	1.5	3	5	7	10
Mixing height, $H_{\text{mix}}/\text{m}^c$	500	500	500	500	230	60	30
Dry deposition residence time, $\tau_{\text{dry}}/\text{s}^d$	$1 \cdot 10^6$ (1.5 wks)	$2 \cdot 10^5$ (2.3 d)	$3.3 \cdot 10^4$ (10 h)	$1.7 \cdot 10^4$ (5 h)	5000 (1.5 h)	850 (15 min)	300 (5 min)
Transport distance, X/km^e	$1 \cdot 10^4$	2000	330	170	50	8.5	3

^a Assumed to have equilibrated at 80% RH.
^b From §4.6.2.
^c Taken to be the lesser of the height of the marine boundary layer height (assumed to be 0.5 km) and z_{50} , the height at which the steady state concentration is 50% of its value at 10 m (§2.9.5).
^d Defined by H_{mix}/v_d
^e Defined by $H_{\text{mix}}U_{10}/v_d$.

Figure 23: Dry deposition residence times for SSA based on r_{80} . Figure taken from Lewis and Schwartz (2004), their Table 8.

The small SSA observed ($r_d \sim 2 \mu\text{m}$) have residence times ~ 10 hrs and could originate from the open ocean. Figure 22b and 22f show that some of the back trajectories from the sampling site pass by Moloka'i and Maui before reaching O'ahu. Therefore, wave breaking along the coastlines of these islands may also be a source for the small SSA observed.

These findings confirm our expectations. The positive correlation between SSA concentration and wave height and wind history, the proximity of our sampling site to the surf zone, the evidence of waves generated by trade wind fetch, and the low residence time of large SSA all imply that locally generated SSA are observed.

4.2 Local Factors

To understand the local production of SSA, the local factors at the sampling site must be further examined. The topography and bathymetry around the sampling location overlain with flight paths created from the GPS data of the iMet-XQ2 instrument at the top of the kite from each sampling day provides more insight (Figure 24). Visible in Figure 24b are two offshore islands near the sampling site; the larger offshore island is Mānana Island, also known as Rabbit Island, and the smaller offshore island is Kāohikaipu Island. These two islands are upwind of the sampling site under trade wind conditions, and therefore wave breaking on their coastlines may be an additional source of SSA in observations.

Because the iMet-XQ2 instrument is at the top of the kite, it can be assumed that all the mini-GNI instruments lie between the iMet-XQ2 instrument and the kite launch point. The position of the iMet-XQ2 instrument can therefore be used to estimate the maximum possible extent that the mini-GNI instruments flew inland from the launch point. The maximum distance inland from the launch point was estimated to be ~280-550 m.

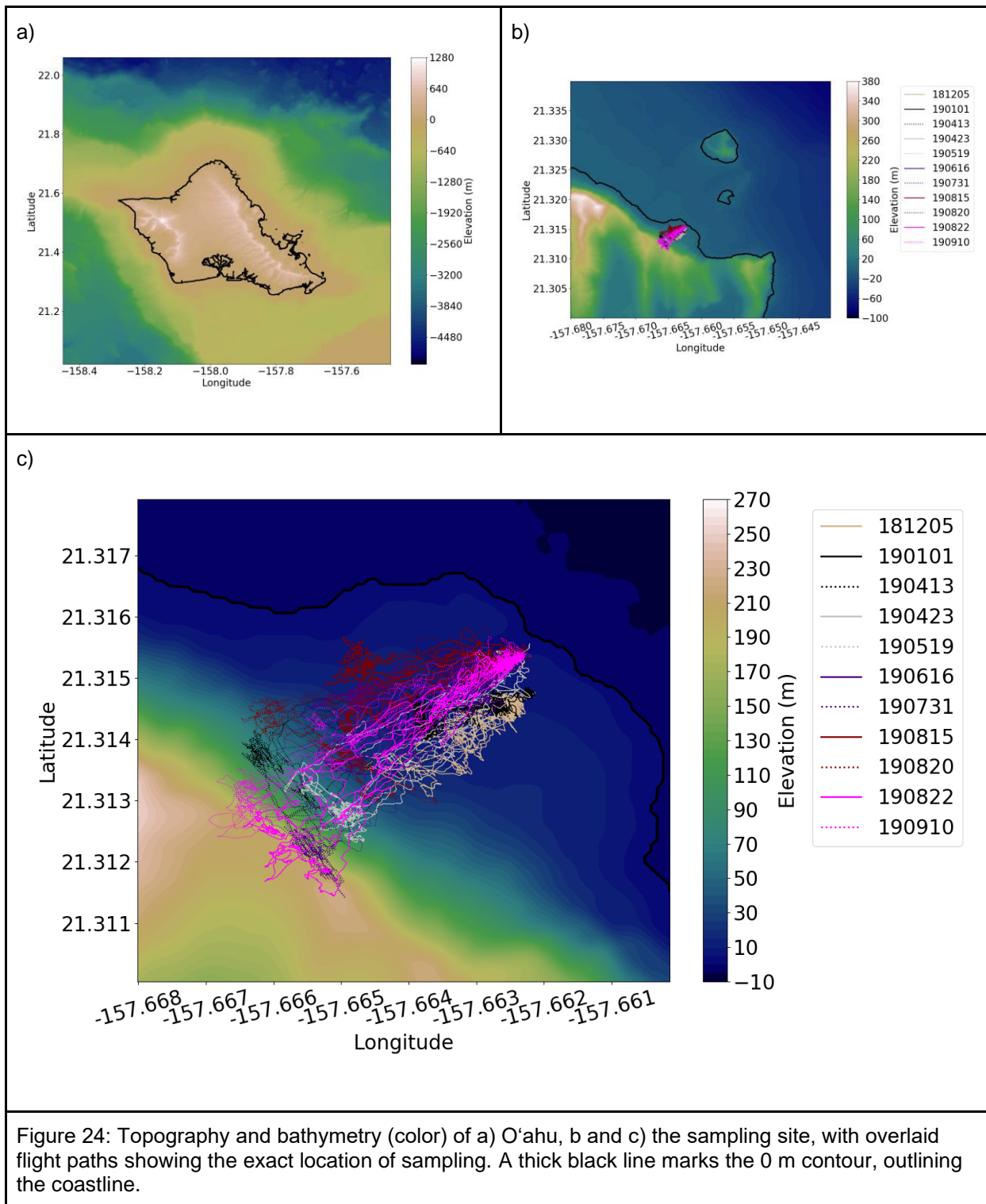


Figure 24: Topography and bathymetry (color) of a) O'ahu, b and c) the sampling site, with overlaid flight paths showing the exact location of sampling. A thick black line marks the 0 m contour, outlining the coastline.

Local bathymetry is important because waves break on interaction with shallow water near land. Tides can therefore affect whether wave breaking is stronger or weaker by changing the depth of the water. At the sampling site, the depth of water increases to nearly 10 m just offshore (Figure 24c) and to more than 60 m past the offshore islands (Figure 24b). This is a rapid change relative to changes in the water level, which, during the sampling periods, ranged from 0-1 m (CO-OPS 2020); in Figure 25, the total SSA concentration is plotted against the tide level, revealing a low correlation (r^2 of 0.07). The change in tides is too small relative to the change in bathymetry just off the shore of the sampling site, and the change in tides therefore correlates poorly with total SSA concentration.

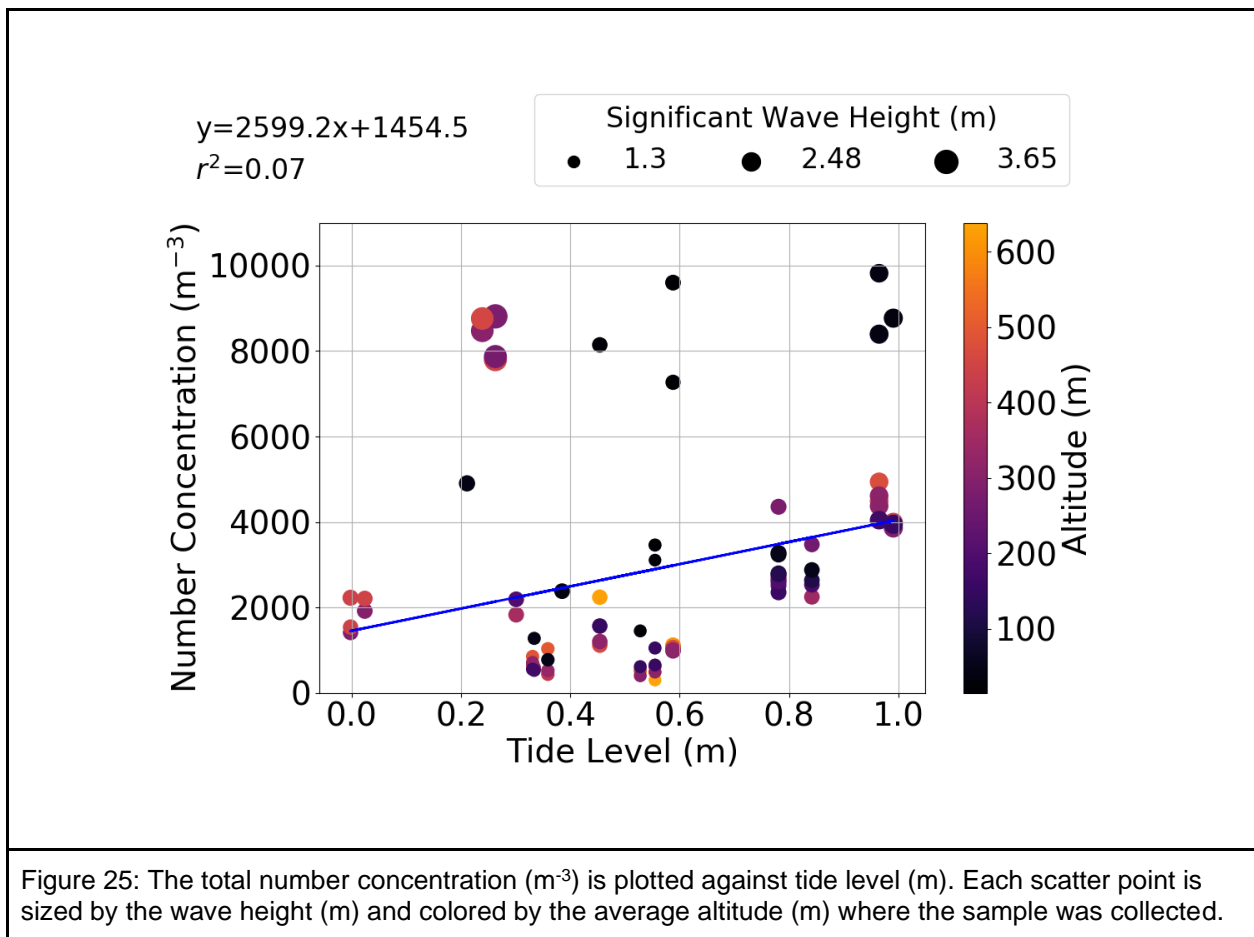


Figure 25: The total number concentration (m^{-3}) is plotted against tide level (m). Each scatter point is sized by the wave height (m) and colored by the average altitude (m) where the sample was collected.

4.3 Lognormal Distribution Fitting

The observed SSA size distributions are fitted to lognormal distributions in order to quantitatively compare them. The SSA size distribution is commonly represented in models with lognormal distributions due to their convenience and reasonable fit (Lewis and Schwartz 2004). The SSA size distribution for each of the mini-GNI samples was fitted to a lognormal distribution using the `lmfit` package (Newville et al. 2019) for Python. The bins were weighed by $1/(1 - CE)$ to ensure that bins with high CE would be more strongly considered than bins with low CE. Figure 26 shows the fit, in red, of two representative samples to the lognormal distribution. While the bin weighting scheme puts high weight on larger sized SSA bins with poor statistics due to their low frequency of occurrence, it is also these larger sized bins that have the highest CE, which was deemed more important in the present analysis.

In general, the observed SSA size distributions fit poorly to the lognormal distribution. Many samples have χ^2 values of over 100, and those that have χ^2 values under 100 still almost all fail a chi-squared goodness-of-fit test. The exceptions are samples 190423a1, 190822a1, 190822a8, and 190822a12. Three of the four samples that fitted well to a lognormal distribution came from the same sample day, 8/22/19. This could be because fewer SSA were captured on 8/22/19 compared to others (Figure 18). Figure 26a shows a large drop off in number concentration as SSA size reaches $10 \mu\text{m}$, leading to a poor lognormal fit. On the other hand, Figure 26b shows nearly an order of magnitude decrease in SSA concentration and a more gradual drop off in SSA concentration with size, fitting better to a lognormal distribution. The poor fit of the observed coastal data to the lognormal distribution could indicate that another representation is needed to represent SSA size distribution in coastal zones, but it could also be an artifact of attempting to fit a small portion ($\sim 2\text{-}16 \mu\text{m}$) of the SSA size distribution to a lognormal distribution.

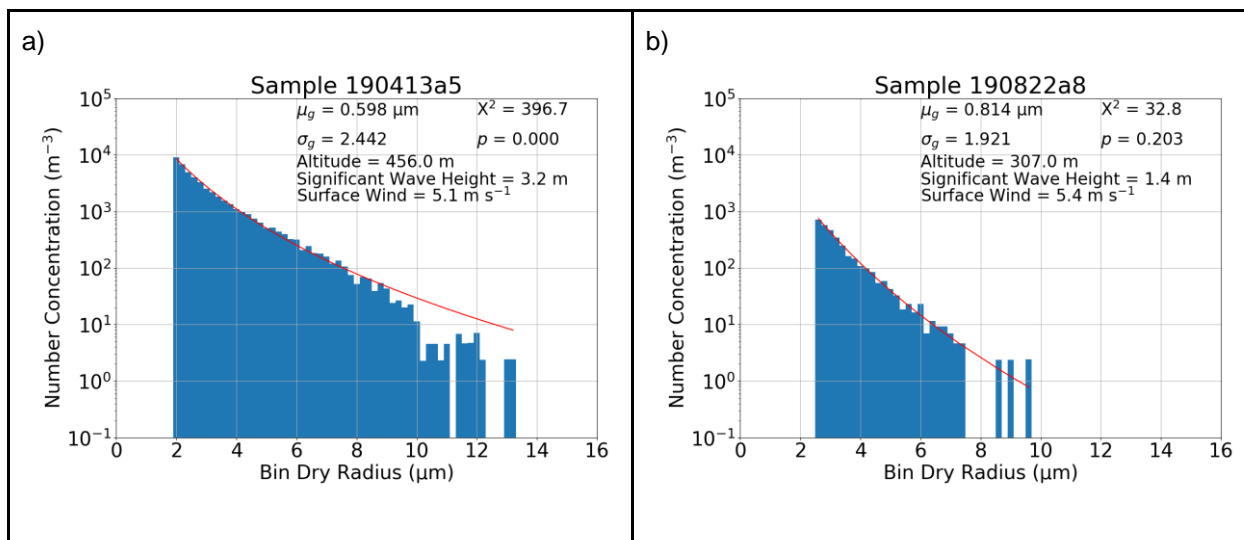


Figure 26: Two examples of SSA size distribution fit with the lognormal distribution from a) 4/13/19 and b) 8/22/19. Listed on each distribution plot are the geometric mean dry radius (μm), the geometric standard deviation, the X^2 value of the fit, and the p-value of the fit.

The lognormal fit data from the mini-GNI was compared to data from the VOCALS-REx campaign (Figure 27). Compared to VOCALS-REx, lower total SSA mass was observed (Figure 27a, b) because our observed SSA samples only captured larger bins ($> 2 \mu\text{m}$), while the VOCALS-REx study could observe smaller and therefore more bins by using aircraft, resulting in higher observed total salt mass.

Larger geometric mean dry radius was observed compared to VOCALS-REx (Figure 27c, d), though the result is suspect due to the observed size distributions fitting poorly to the lognormal distribution. The software often returned large values ($> 1.5 \mu\text{m}$) for geometric mean dry radius, likely because it had no information about small SSA ($< 2 \mu\text{m}$). An imposed upper bound for the geometric mean dry radius was decided against because it resulted in many size distributions reporting a geometric mean dry radius value equal to that upper bound.

Finally, a very similar distribution of geometric standard deviation to VOCALS-REx was found (Figure 27e, f). This indicates that the shape of the observed size distributions is similar to those of VOCALS-REx, reinforcing the idea in Chapter 3 that the present study was able to capture real SSA size distributions. This also reinforces results from Clarke et al. (2006), which concludes that the sea salt aerosol size distribution shape from the shorebreak is similar to that from the open ocean.

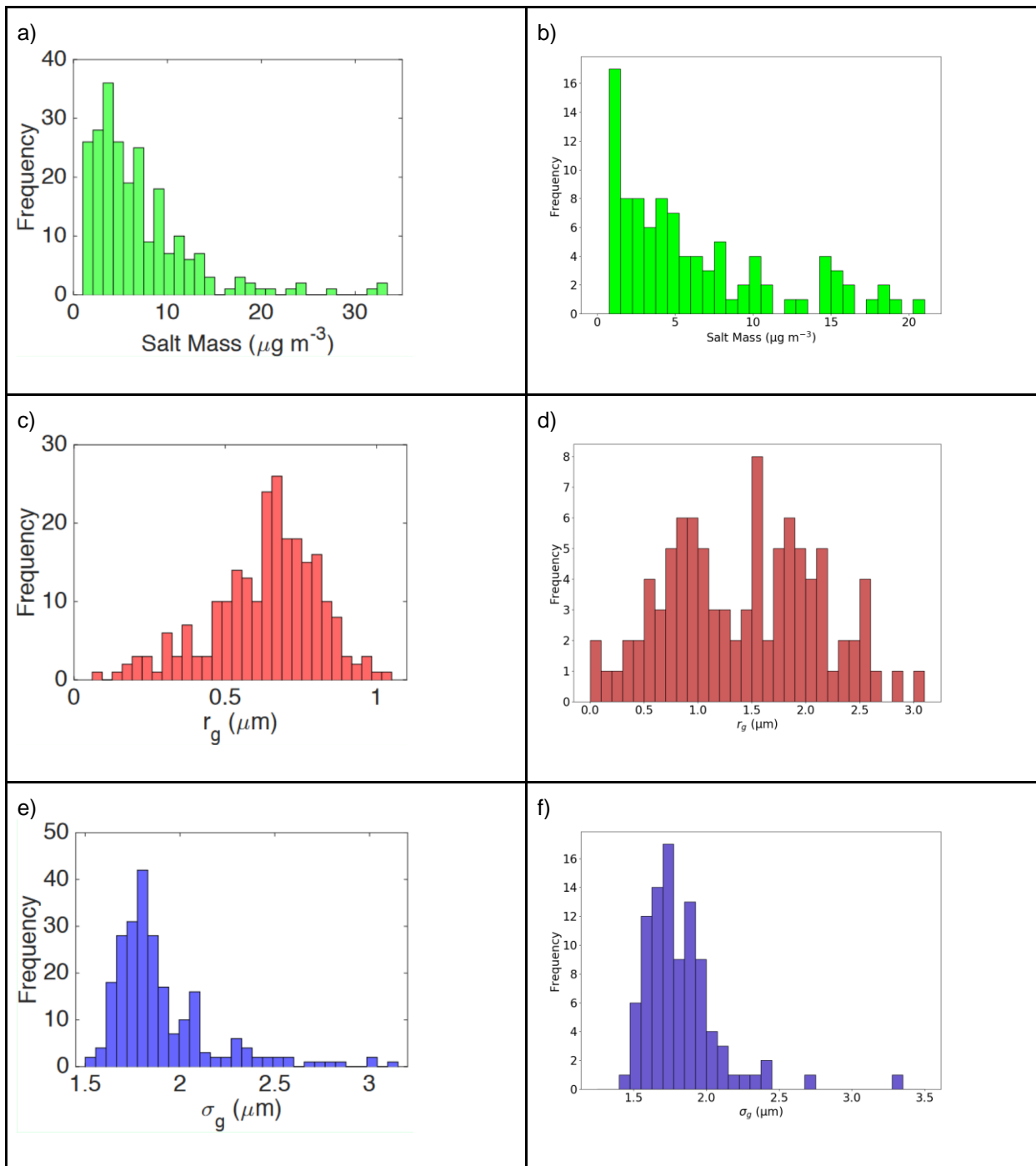


Figure 27: The distributions for total salt mass (top row), geometric mean radius (middle row), and geometric standard deviation (bottom row) observed over the open ocean by the GNI during VOCALS-REx (left column) and along the O'ahu coastline by the mini-GNI (right column).

4.4 Wind Sensitivity Study

To examine the sensitivity of the results with respect to the wind speed measurements, the two anemometers were deployed at the SSA sampling location on 2019 Oct 3. The sampling occurred during a period of strong trade winds, so the wind profile was assumed to be representative of a typical sampling day. The two anemometers were attached to the kite string with 5 m of kite string between them. They were deployed at various altitudes for 10 min increments to obtain a vertical profile of wind speed at 3 Hz resolution, captured over nearly 4 hrs, during which surface winds stayed within a 3 m s^{-1} range.

The anemometer observations were found to conform more closely to log law behavior. The data was fit to an empirical log law,

$$u = 1.062098 \ln(z) + 2.027672 \quad (\text{Eq. 9}),$$

and compared with the anemometer observations and the power law wind profile estimation (Figure 28).

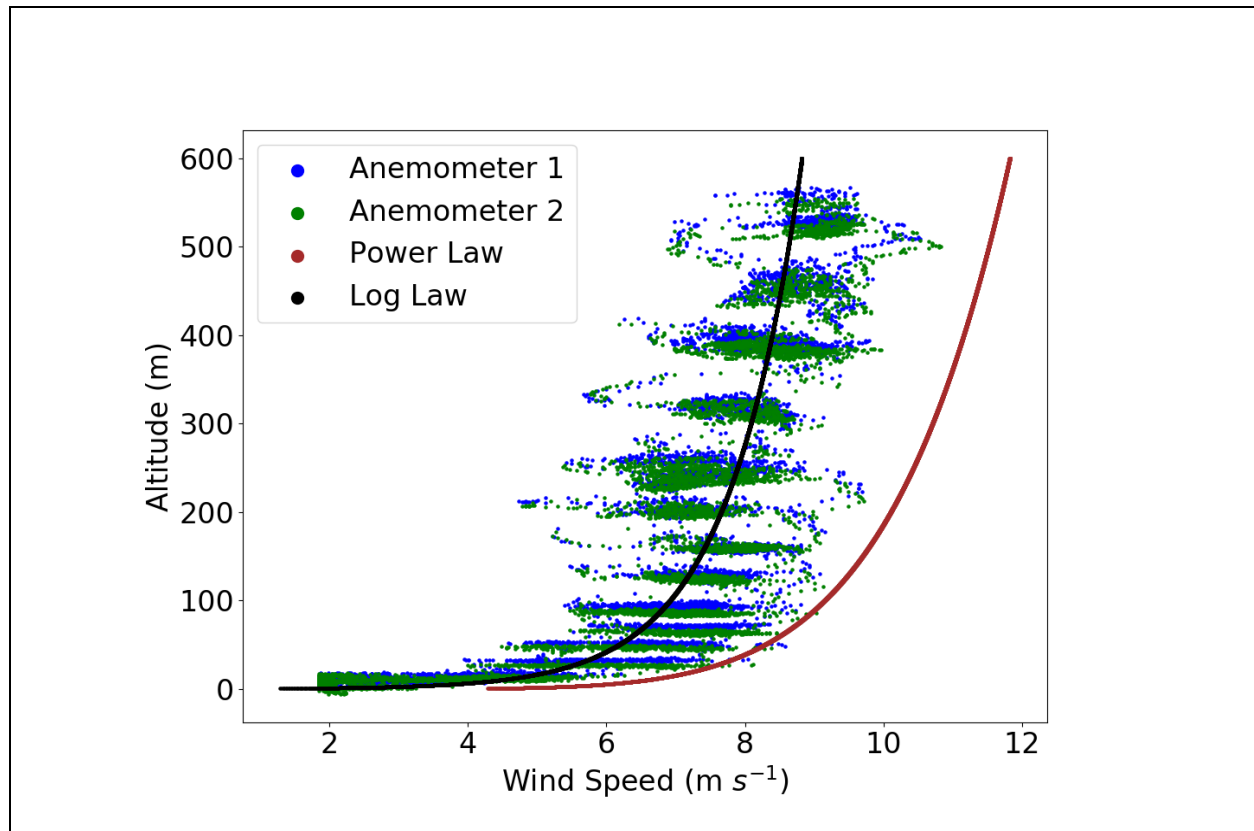


Figure 28: Vertical wind profile (all m s^{-1}) of observation data from two anemometers (green and blue dots) are plotted along with the power law wind profile and a log law wind profile fitted to the observation data.

Manipulating the fitted log law into the form of the wind profile log law results in the following equation:

$$u = 1.062098 \ln \left(\frac{z}{0.148211} \right) \quad (\text{Eq. 10}),$$

where

$$1.062098 = \frac{u_r}{\ln(z_r/z_0)} \quad (\text{Eq. 11}),$$

and u_r and z are the wind speed at a reference height and the reference height respectively.

The roughness parameter z_0 is therefore approximately 0.148, which corresponds to “few trees, summer time” according to Arya (2001, Figure 29). This is reasonable given that our sampling site has various trees and bushes and that it is inclined from the nearby flat shoreline.

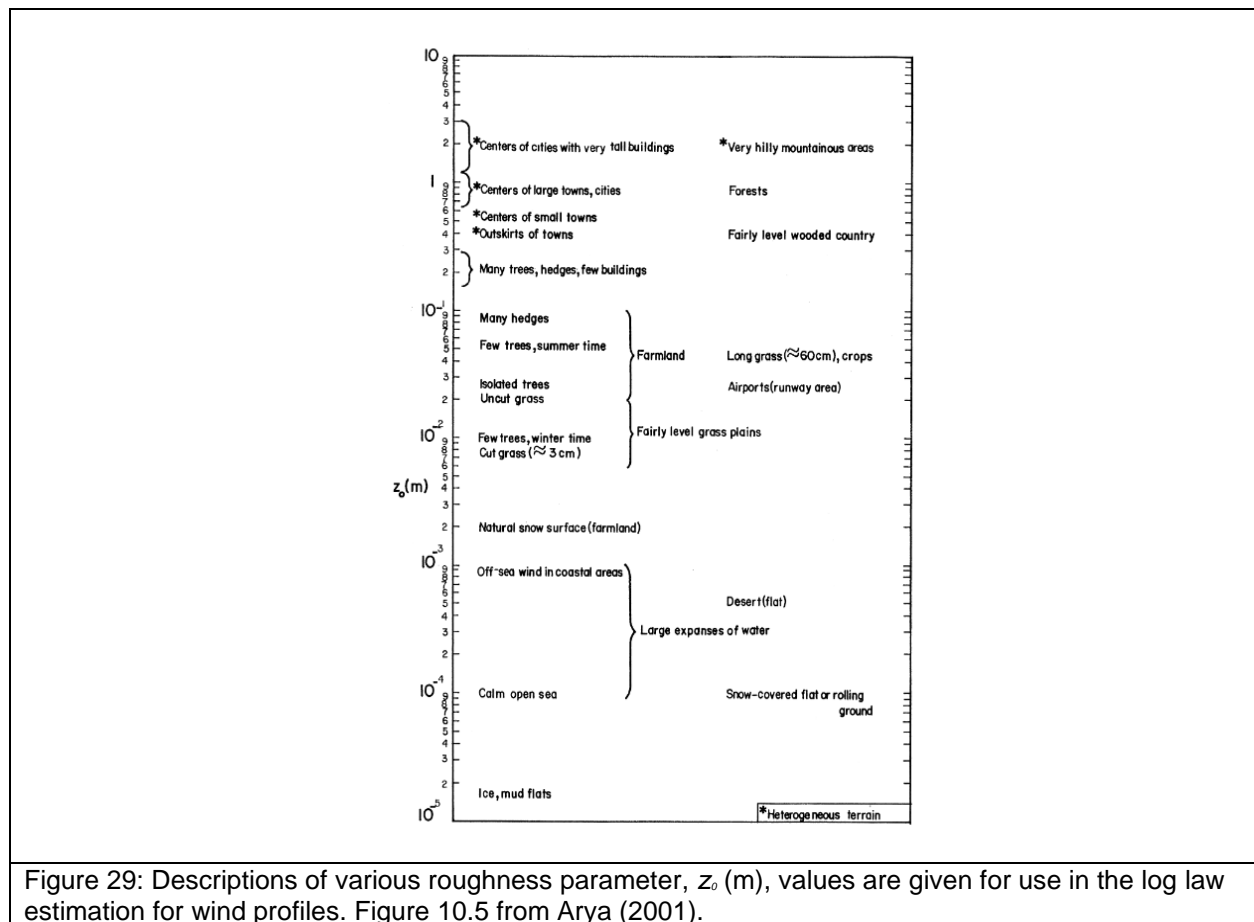


Figure 29: Descriptions of various roughness parameter, z_0 (m), values are given for use in the log law estimation for wind profiles. Figure 10.5 from Arya (2001).

Due to the uncertainty in surface wind measurements, definitive values of u_r and z_r cannot be assigned. On the wind sampling day, the two anemometers were placed between and below two Kestrels to obtain surface wind measurements. Over the course of ~10 minutes, the anemometers measured an average of 3.81 and 3.99 m s⁻¹ while the two Kestrels measured 5.0 and 4.8 m s⁻¹ over the same time period. The cause of this discrepancy is unknown and could be the result of their slightly different positions or due to the effect of the 3D casing on the anemometers. As the Kestrels are used to obtain surface wind measurements for all our samples, it seems prudent to assign these values based on the Kestrel-observed surface wind measurements of 5.0 and 4.8 m s⁻¹. Thus, u_r is 5.4 m s⁻¹, and z_r is 23.9 m. It was earlier stated that our Kestrels were placed about 6 m above the level of the ocean, so the resulting z_r value is not physical. This could be caused by complications in the terrain due to the incline from the flat shoreline to the sampling location.

Comparing the empirically derived log law to the power law used in this study to estimate wind aloft reveals that our wind estimates need to be decreased by ~30-35% to match the anemometer-observed wind profile (Figure 28). This result is not absolute because it is based on a wind profile from a single day. It is unknown whether the wind profile obtained is representative of a typical sampling day or if the wind profile is even consistent between sampling days.

A sensitivity study was therefore conducted to investigate the effects of decreasing wind speed by 35% on the size distribution. This was accomplished by changing the wind speed in the calculation required to obtain number concentration from the raw count on each slide (Equation 1).

Changing the wind speed clearly changes the sample volume and the CE. Decreasing the wind speed results in decreased sample volume and decreased CE, leading to a higher calculated number concentration. An example result for decreasing the wind speed by 35% is shown in Figure 30. Only one example is shown because the effect is the same for all the size distributions observed. The effect of decreasing wind by 35% results in an increase in number concentration by a factor of 1.5-2 (Figure 30b).

Another effect of decreasing the wind speed is that the 40% CE cutoff size increases from 3.9 to 4.9 μm . The analyses from Chapter 3 were rerun using a cut off of 4.9 μm , and the conclusions were unchanged.

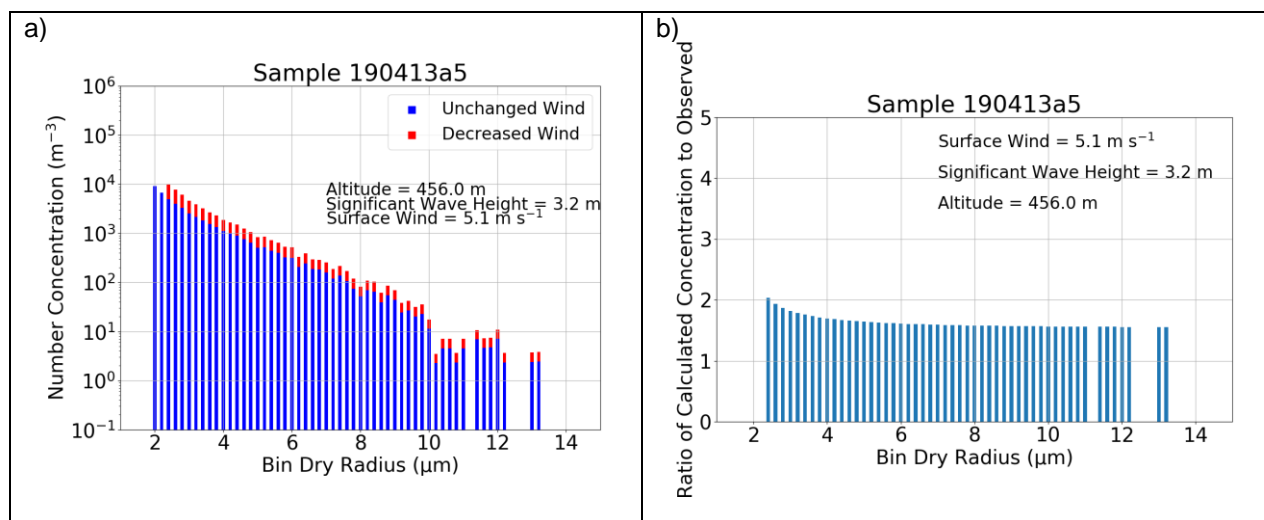


Figure 30: a) The effect of changing wind speed on an example SSA size distribution. In blue is the original size distribution and in red is the effect of decreasing the wind estimate by 35%. b) The ratio of the concentration calculated from decreasing wind by 35% to the observed concentrations (red vs blue histogram in a) is plotted.

4.5 Other Uncertainties

4.5.1 Relative Humidity

In Section 4.1, it was determined that the SSA observed are likely locally generated. Because of this, the mini-GNI is potentially observing SSA closer to formation size rather than equilibrium size which adds an additional layer of complication that needs to be considered. The formation radius r_{90} is estimated to be four times the dry radius (Lewis and Schwartz 2004). This is particularly a concern for samples near the surface because the radius relaxation time, or the time required for the radius to drop to 1/e fraction of its initial value, is on the order of seconds to minutes (Figure 31, Veron 2015).

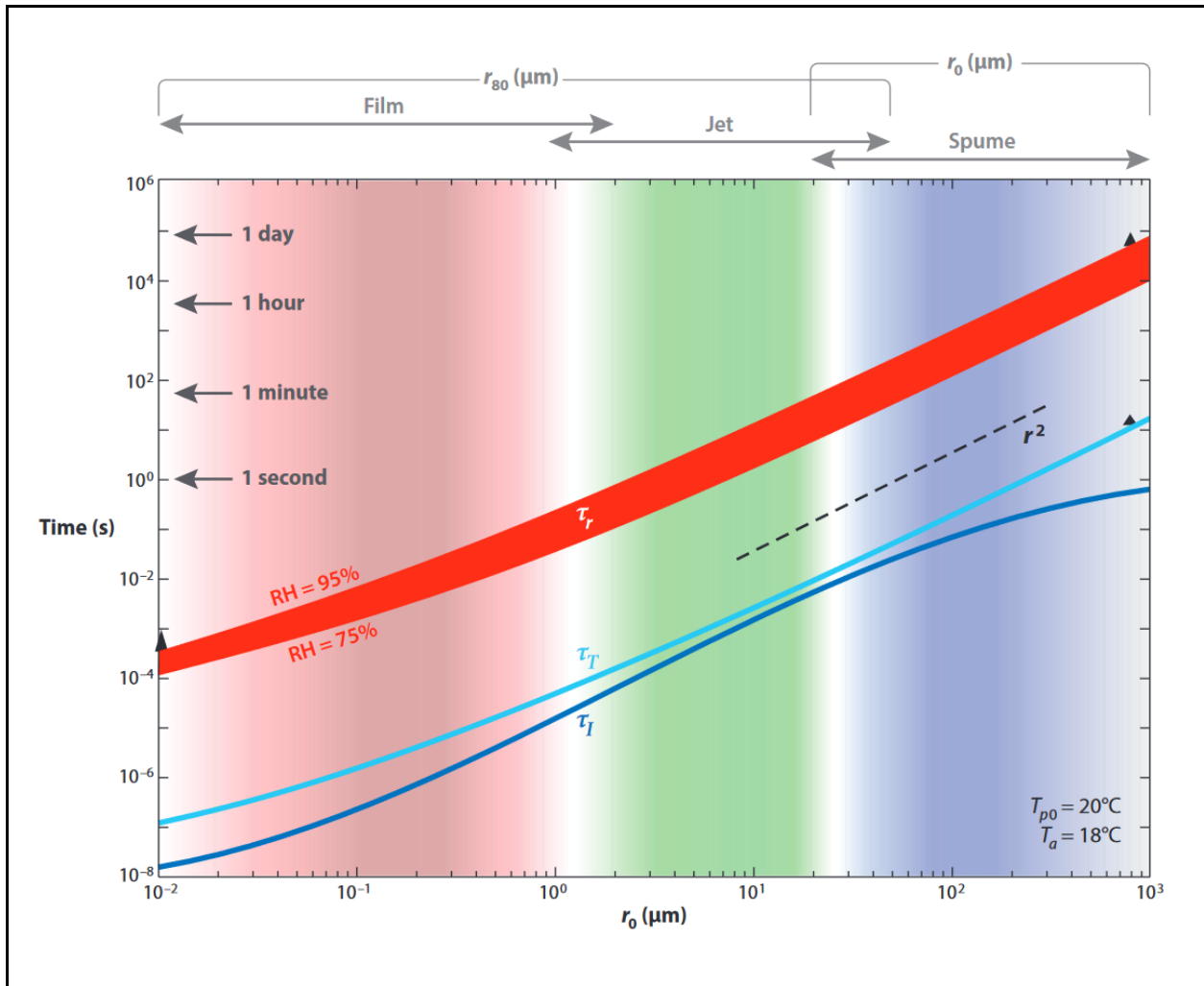


Figure 31: Relaxation time (s) for drop radius (red), drop temperature (blue), and drop inertia (cyan) is plotted as a function of the drop's initial radius, r_0 (μm). Figure 4 from Veron (2015).

For near-surface samples, the observed SSA may be near formation size, resulting in higher CE, meaning that the number concentration is overestimated. This only applies to bins of large SSA ($r_{80} \sim 100 \mu\text{m}$) because smaller droplets ($r_{80} \sim 10 \mu\text{m}$) have a relaxation time on the order of seconds. However, large particles ($r_{80} \sim 100 \mu\text{m}$) already have a high CE that would increase by a small amount ($\sim 1.6\%$) with increasing size (Table 1). Meanwhile, small particles ($r_{80} \sim 10 \mu\text{m}$), that have significantly increasing CE ($\sim 19.7\%$) with increasing size, equilibrate too quickly to be sampled at formation size.

Dry radius (μm)	Equilibrium radius (μm)	Formation radius (μm)	CE at equilibrium radius	CE at formation radius
4	8	16	71.8%	91.5%
16	32	64	97.8%	99.4%

Table 1: The difference in CE between particles at equilibrium (with 80% RH) radius and at formation radius.

4.5.2 Orientation

The orientation of the mini-GNI as it flies on the kite string is another source of uncertainty. The position of the mini-GNI is measured by an orientation sensor in Euler angles relative to the initial position when the mini-GNI is first powered on. Using the orientation sensor, it is therefore possible to determine the range of movement the sensor experiences during sampling. A brief depiction of Euler angles is shown in Figure 32 (Schwab and Meijaard 2006).

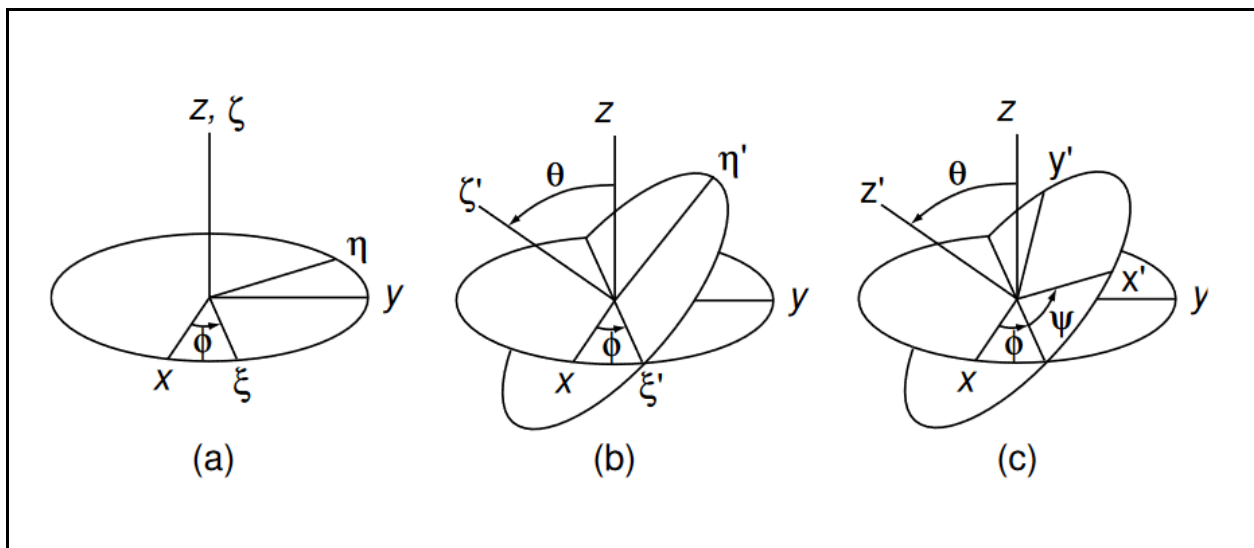
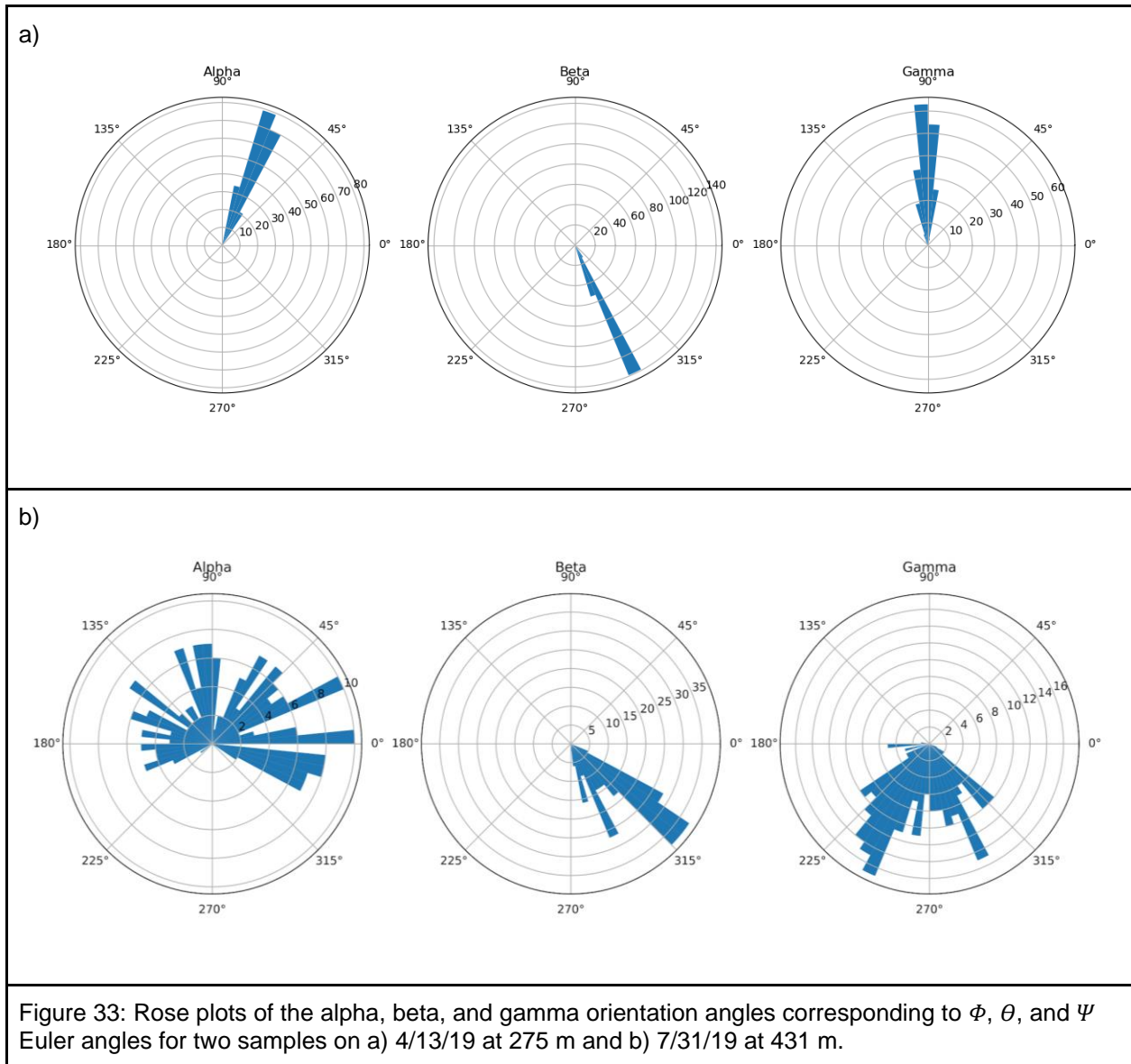


Figure 32: The three stages of Euler angle rotation: a) ϕ , b) θ , and c) ψ . Figure 1 from Schwab and Meijaard (2006).

The Euler rotation angles ϕ , θ , and ψ are labeled as alpha, beta, and gamma respectively in Figure 33 to describe the mini-GNI orientation. Orientation rose plots from 4/13/19 and 7/31/19 are shown in Figure 33 as an example. Most samples have orientation similar to that of Figure 33a, which shows that the orientation of the mini-GNI stays within 5-10°. However, eight samples had very unsteady orientation, with the worst sample shown in Figure 33b. One sample was unsteady in only the alpha angle, five

samples were unsteady in only the gamma angle, and two samples, including the one shown in Figure 33b, were unsteady in both the alpha and gamma angle. These samples were not removed from the analyses in Chapter 3 because it is unclear whether these large variations are due to a real change in wind or are relative to the wind.



Chapter 5: Summary and Conclusions

In this study, a kite platform was used to sample SSA size distributions on the windward coastline of O'ahu. The results established that the kite platform is a valid method for sampling SSA size distribution. The results were compared to those from VOCALS-REx, where SSA size distribution was sampled from an aircraft platform. It was found that our SSA size distributions have a similar shape to the VOCALS-REx size distributions.

Environmental variables that influence SSA size distribution were examined. Our results were first compared to Woodcock (1953), which found that SSA concentration increases with increasing wind force and decreases with increasing altitude, and Blanchard et al. (1984), which found that SSA concentration decreases sharply between 19.5-30 m. Our SSA size distributions were well-mixed up to about 450 m, including within the lowest 30 m, and then decreased in overall concentration above 600 m, and up to our highest altitude (~700 m) samples.

No relationship was found between SSA concentration and instantaneous wind speed, contrary to the results of Woodcock (1953) and model parameterizations that give SSA production based on wind speed. It was hypothesized that this contradiction is due to the choice of sampling location. The present study is a coastal study while Woodcock's study was performed over the open ocean, and model parameterizations are designed to represent SSA over the open ocean. Wave breaking along a coastline is more dependent on local factors than on wind speed, so it was hypothesized that the observed SSA were locally generated. To examine this hypothesis, other variables that could influence SSA size distribution were examined.

Because SSA are generated by wave breaking, it was reasoned that larger waves would result in more energetic wave breaking, producing more and larger SSA. Indeed, a positive correlation was found between SSA concentration and significant wave height. Given that large waves are produced by a large and enduring fetch, the wind history for each sample was also investigated, and a positive correlation was found between wind history and SSA concentration. Examining HySPLIT back trajectories confirmed that nearly all samples were taken with trade wind conditions occurring both during sampling and prior to sampling. Finally, the low residence time (minutes to hours) of the observed SSA size distribution

provided further evidence that locally generated SSA are observed due to the speed at which SSA are lofted.

In summary, the non-correlation between SSA concentration and instantaneous wind speed, the positive correlations between SSA concentration and wave height and wind history, the HySPLIT back trajectories, and the residence time of the observed SSA all suggest that the SSA size distribution in Hawai'i is locally driven. As such, SSA size distribution along the coastline is dependent on different variables than the SSA size distribution over the open ocean.

Additional future work can improve the sampling technique and to investigate further. For example, a drone can be used to sample SSA with the mini-GNI beyond the reef over the open ocean at low altitudes to find potential differences between SSA concentrations over open ocean and over the coastal zone. Flying a drone with the mini-GNI from a boat or ship could also be used to sample over the open ocean, though flying the kite from a ship was attempted but proven impractical. Furthermore, a primary limitation to this study was the low CE due to the reliance on wind speed alone. To increase CE, a method to sample with the mini-GNI with a flying UAS should be explored.

Chapter 6: References

- Adafruit: AM2302 (wired DHT22) temperature-humidity sensor. Accessed 28 February 2020, <https://www.adafruit.com/product/393>
- Adafruit: MPL3115A2 - I2C barometric pressure/altitude/temperature sensor. Accessed 28 February 2020, <https://www.adafruit.com/product/1893>
- Arya, S. P., 2001: *Introduction to Micrometeorology*. Academic Press, 420 pp.
- Banta, R. M., 1990: The role of mountain flows in making clouds. *Atmospheric Processes over Complex Terrain, Meteor. Monogr.*, No. 23, Amer. Meteor. Soc., 229-283.
- Blanchard, D. C., A. H. Woodcock, and R. J. Cipirano, 1984: The vertical distribution of the concentration of sea salt in the marine atmosphere near Hawai'i. *Tellus B*, **36**, 118-125.
- Blyth, A. M., S. G. Lasher-Trapp, W. A. Cooper, C. A. Knight, and J. A. Latham, 2003: The role of giant and ultragiant nuclei in the formation of early radar echoes in warm cumulus clouds. *J. Atmos. Sci.*, **60**, 2557-2572.
- Campuzano-Jost, P., C. D. Clark, H. Maring, D. S. Covert, S. Howell, V. Kasputin, K. A. Clarke, E. S. Saltzman, and A. J. Hynes, 2003: Near-real-time measurement of sea-salt aerosol during the SEAS campaign: Comparison of emission-based sodium detection with an aerosol volatility technique. *J. Atmos. Oceanic Technol.*, **20**, 1421-1430.
- Clarke, A. D., S. R. Owens, and J. Zhou, 2006: An ultrafine sea-salt flux from breaking waves: Implications for cloud condensation nuclei in the remote marine atmosphere. *J. Geophys. Res.*, **111**, 14 pp.
- CO-OPS, 2020: Observed water levels at 1612480, Mokuoloe, HI. National Water Level Observation Network, accessed 27 March 2020.
- Daniels, A., 1989: Measurements of atmospheric sea salt concentrations in Hawai'i using a Tala kite. *Tellus B*, **41**, 196-206.

- de Leeuw, G., E. L. Andreas, M. D. Anguelova, C. W. Fairall, E. R. Lewis, C. O'Dowd, M. Schulz, and S. E. Schwartz, 2011: Production flux of sea spray aerosol. *Rev. Geophys.*, **49**, 39 pp.
- Feingold, G., W. R. Cotton, S. M. Kreidenweis, and J. T. Davis, 1999: The impact of giant cloud condensation nuclei on drizzle formation in stratocumulus: Implications for cloud radiative properties. *J. Atmos. Sci.*, **56**, 4100-4117.
- Google Maps, 2019: Google Maps satellite view of O'ahu. Retrieved 19 August 2019.
- Houghton, H.G., 1938: Problems connected with the condensation and precipitation processes in the atmosphere. *Bull. Amer. Meteor. Soc.*, **19**, 152-159.
- IPCC, 2013: Climate change 2013: The physical science basis. Contribution of working group 1 to the Fifth Assessment Report of the Intergovernmental Panel on Climate Change [Stocker, T.F., D. Qin, G.-K. Plattner, M. Tignor, S.K. Allen, J. Boschung, A. Nauels, Y. Xia, V. Bex and P.M. Midgley (eds.)]. Cambridge University Press, Cambridge, United Kingdom and New York, NY, USA, 1535 pp.
- Jaegle, L., P. K. Quinn, T. S. Bates, B. Alexander, and J.-T. Lin, 2011: Global distribution of sea salt aerosols: new constraints from in situ and remote sensing observations. *Atmos. Chem. Phys.*, **11**, 3137-3157.
- Jensen, J. B., and S. Lee, 2008: Giant sea-salt aerosols and warm rain formation in marine stratocumulus. *J. Atmos. Sci.*, **65**, 3678-3694.
- Jensen, J. B., and A. D. Nugent, 2017: Condensational growth of drops formed on giant sea-salt aerosol particles. *J. Atmos. Sci.*, **74**, 679-697.
- Jensen, J. B., S. P. Beaton, J. L. Stith, K. Schwenz, M. Colon-Robles, R. M. Rauber, and J. Gras, 2020a: The Giant Nucleus Impactor (GNI) - A system for the impaction and automated optical sizing of giant aerosol particles with emphasis on sea salt. Part 1: Basic instrument and algorithms. Manuscript submitted to *J. Atmos. Oceanic Technol.*

- Jensen, J. B., S. P. Beaton, D. C. Rogers, J. L. Stith, K. Schwenz, M. Colon-Robles, R. M. Rauber, and J. Gras, 2020b: The Giant Nucleus Impactor (GNI) - A system for the impaction and automated optical sizing of giant aerosol particles with emphasis on sea salt. Part 2: Uncertainty analysis and high-speed drop impact effects. Manuscript in preparation.
- Johnson, D. B., 1980: The influence of cloud-base temperature and pressure on droplet concentration. *J. Atmos. Sci.*, **37**, 2079-2085.
- Johnson, D. B., 1982: The role of giant and ultragiant aerosol particles in warm rain initiation. *J. Atmos. Sci.*, **39**, 448-460.
- Kestrel, 2015: Kestrel Certificate of Conformity. Accessed 30 March 2020, https://cdn.shopify.com/s/files/1/0084/9012/t/11/assets/5000_Certificate_of_Conformity_specs.pdf
- Khairoutdinov, M. and Y. Kogan, 2000: A new cloud physics parameterization in a large-eddy simulation model of marine stratocumulus. *Mon. Wea. Rev.*, **128**, 229-243.
- Lasher-Trapp, S., and J. P. Stachnik, 2007: Giant and ultragiant aerosol particle variability over the Eastern Great Lakes region. *J. Appl. Meteor. Climatol.*, **46**, 651-659.
- Lewis, E. R., and S. E. Schwartz, 2004: Sea salt aerosol production: Mechanisms, methods, measurements, and models - A critical review. *AGU Geophys. Monogr. Ser.*, **152**, 413pp.
- McManus, M., 2014: PacIOOS Wave Buoy 098: Mokapu Point, O'ahu, Hawai'i. Pacific Islands Ocean Observing System, accessed 6 November 2019.
- McNaughton, C.S, and Coauthors, 2007: Results from the DC-8 Inlet Characterization Experiment (DICE): Airborne versus surface sampling of mineral dust and sea salt aerosols. *Aerosol Sci. Technol.*, **41**, 136-159.
- Mechoso, C. R., and Coauthors, 2014: Ocean-Cloud-Atmosphere-Land interactions in the Southeastern Pacific: The VOCALS program. *Bull. Amer. Meteor. Soc.*, **95**, 357-375.
- National Weather Service: PHNG Data. National Weather Service, accessed 16 September 2019.

- Newville, M., and Coauthors: 2019: Imfit/Imfit-py 1.0.0. *Zenodo*. doi:10.5281/zenodo.3588521
- NCEI, 2020: O'ahu, Hawai'i 1/3 arc-second MHW coastal digital elevation model. National Center for Environmental Information, accessed 27 March 2020.
- Parrella, J. P., and Coauthors, 2012: Tropospheric bromine chemistry: Implications for present and pre-industrial ozone and mercury. *Atmos. Chem. Phys.*, **12**, 6723-6740.
- Peterson, E. W., and J. P. Hennessey Jr., 1978: On the use of power laws for estimates of wind power potential. *J. Appl. Meteor. Climatol.*, **17**, 390-394.
- Porter, J. N., B. R. Lienart, and S. K. Sharma, 2000: Using horizontal and slant lidar measurements to obtain calibrated aerosol scattering coefficients from a coastal lidar in Hawai'i. *J. Atmos. Oceanic Technol.*, **17**, 1445-1454.
- Porter, J. N., B. R. Lienart, S. K. Sharma, E. Lau, and K. Horton, 2003: Vertical and horizontal aerosol scattering fields over Bellows Beach, O'ahu, during the SEAS Experiment. *J. Atmos. Oceanic Technol.*, **20**, 1375-1387.
- Ranz, W. E., and J. B. Wong, 1952: Impaction of dust and smoke particles. *Ind. Eng. Chem. Res.*, **44**, 1371-1381.
- Rolph, G. D., A. F. Stein, and B. J. B. Stunder, 2017: Real-time Environmental Applications and Display System: READY. *Environ. Model. Softw.*, **95**, 210-228.
- Saiz-Lopez, A., and R. von Glasow, 2012: Reactive halogen chemistry in the troposphere. *Chem. Soc. Rev.*, **41**, 6448-6472.
- Savoie, D. L., and J. M. Prospero, 1977: Aerosol concentration studies for the northern tropical Atlantic. *J. Geophys. Res.*, **82**, 5954-5964.
- Schwab, A. L., and J. P. Meijaard, 2006: How to draw Euler angles and utilize Euler parameters. *Proc. of IDETC/CIE 2006*, Philadelphia, PA, American Society of Mechanical Engineers.

- Stein, A. F., R. R. Draxler, G. D. Rolph, B. J. B. Stunder, M. D. Cohen, and F. Ngan, 2015: NOAA's HYSPLIT atmospheric transport and dispersion modeling system. *Bull. Amer. Meteor. Soc.*, **96**, 2059-2077.
- Tang, I. N., A. C. Tridico, and K. H. Fung, 1997: Thermodynamic and optical properties of sea salt aerosols. *J. Geophys. Res.*, **102**, 23269-23275.
- Twomey, S., 1977: The influence of pollution on the shortwave albedo of clouds. *J. Atmos. Sci.*, **34**, 1149-1152.
- Watson, C. D., R. B. Smith, and A. D. Nugent, 2015: Processes controlling precipitation in shallow, orographic, trade wind convection. *J. Atmos. Sci.*, **72**, 3051-3072.
- Wilson, J. C., and Coauthors, 2004: Function and performance of a low turbulence inlet for sampling supermicron particles from aircraft platforms. *Aerosol Sci. Technol.*, **38**, 790-802.
- Woodcock, A. H., and M. M. Gifford, 1949: Sampling atmospheric sea-salt nuclei over the ocean. *J. Mar. Res.*, **8**, 177-197.
- Woodcock, A. H., 1952: Atmospheric salt particles and raindrops. *J. Meteor.*, **9**, 200-212.
- Woodcock, A. H., 1953: Salt nuclei in marine air as a function of altitude and wind force. *J. Meteor.*, **10**, 362-371.

Chapter 7: Appendix

7.1 Mini-GNI 3D Design

The casing of the mini-GNI was designed using Autodesk® Fusion 360™. The 3D diagram is shown from the side in Figure A1a and from the top in Figure A1b. In both views, the Micro Servo is shown in its position in pale blue. The other sensors are attached by screws where screw holes are depicted. This will be shown in more detail in Section 7.2.

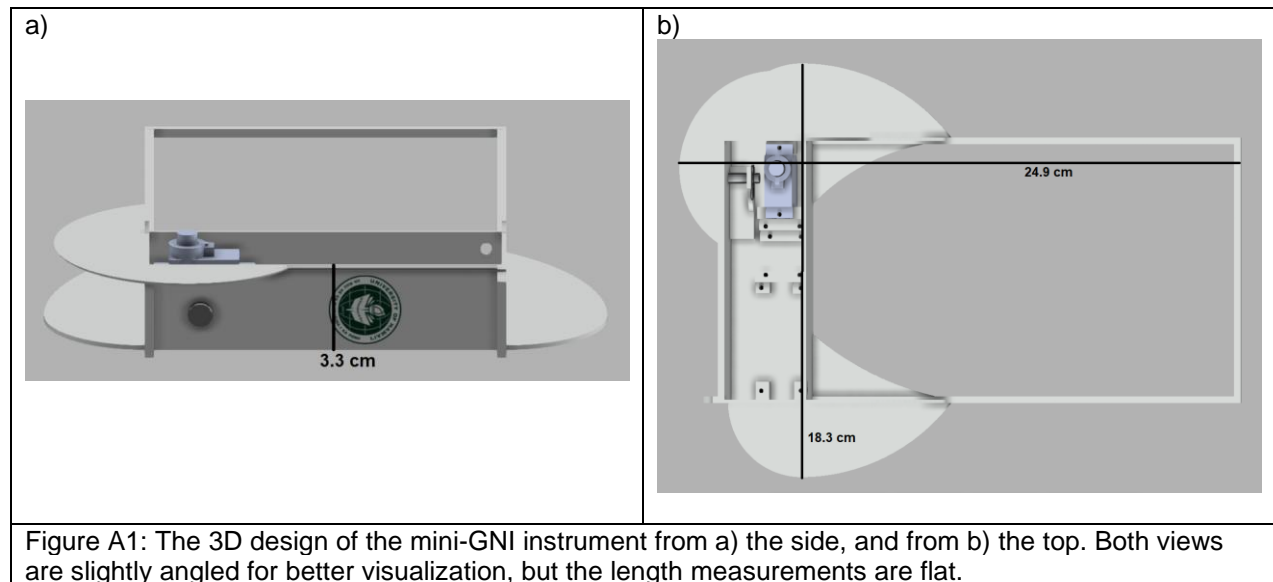


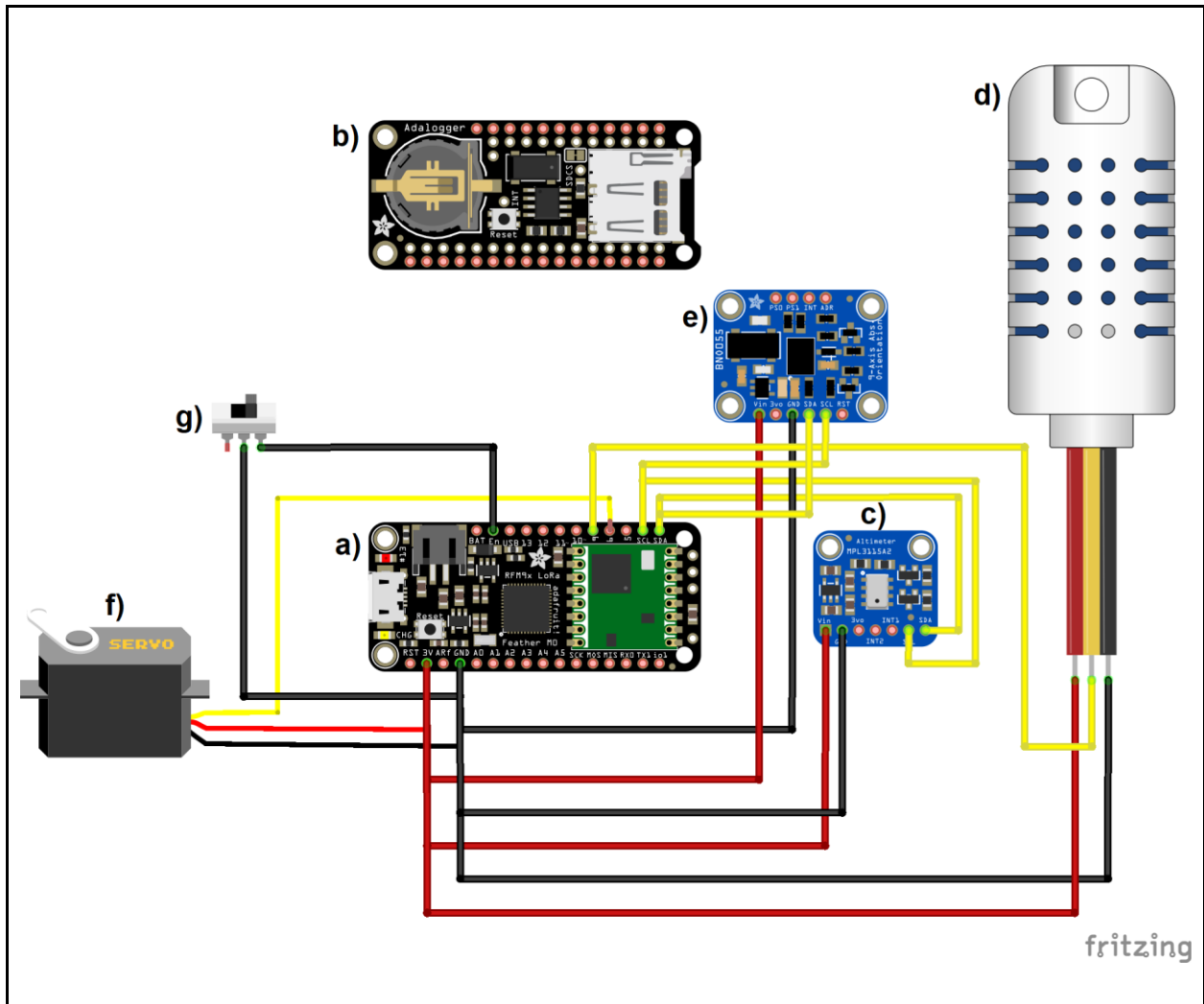
Figure A1: The 3D design of the mini-GNI instrument from a) the side, and from b) the top. Both views are slightly angled for better visualization, but the length measurements are flat.

7.2 Mini-GNI Assembly

The required materials to assemble the mini-GNI are detailed in Table A1. The components are assembled according to the wiring diagram in Figure A1.

Part Name	Adafruit Part Number	Figure A1 label
Adafruit Feather M0 with RFM95 LoRa Radio	3178	a
Adalogger FeatherWing with RTC + SD Add-on	2922	b
MPL3115A2 - I2C Barometric Pressure/Altitude/Temperature Sensor	1893	c
AM2302 (wired DHT22) Temperature-Humidity Sensor	393	d
9-DOF Absolute Orientation IMU Fusion Breakout - BNO055	2472	e
Micro Servo	169	f
SPDT Slide Switch	805	g
Lithium Ion Polymer Battery - 3.7V 150mAh	1317	
CR1220 12mm Diameter 3V Lithium Coin Cell Battery	380	
Female Header Set	2886	

Table A1: Adafruit parts list for building the mini-GNI.



A1: The wiring diagram for the mini-GNI, made with Fritzing. Black wires connect to ground, red wires connect to power, and yellow wires are for other functions.

The components are placed into the 3D case, resulting in the final design depicted in Figure 7. A step by step process of placing each component in its place is detailed in Figures A2-A8.

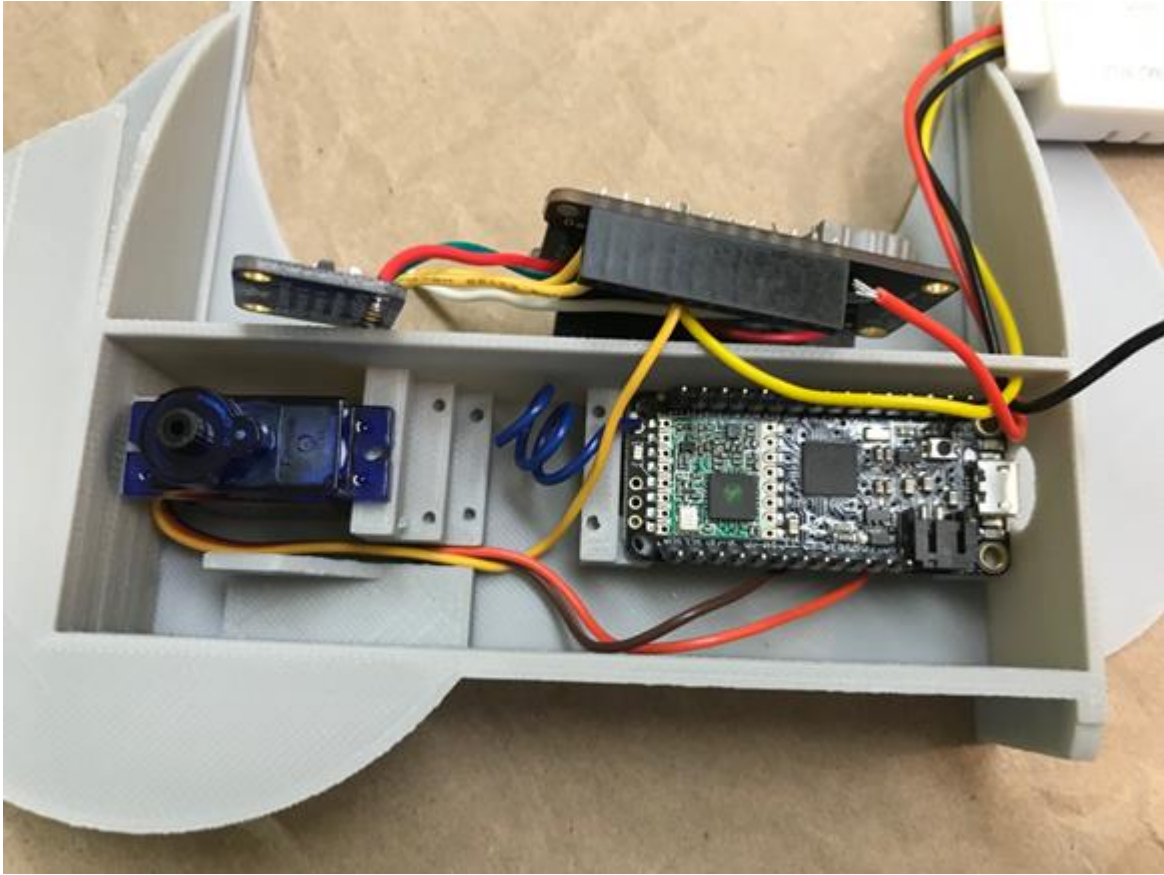


Figure A2: The Micro Servo and the Feather M0 are placed into position. The Adalogger FeatherWing and the MPL3115A2 are wired but not put in place.



Figure A3: The Adalogger FeatherWing has been attached to the Feather M0.

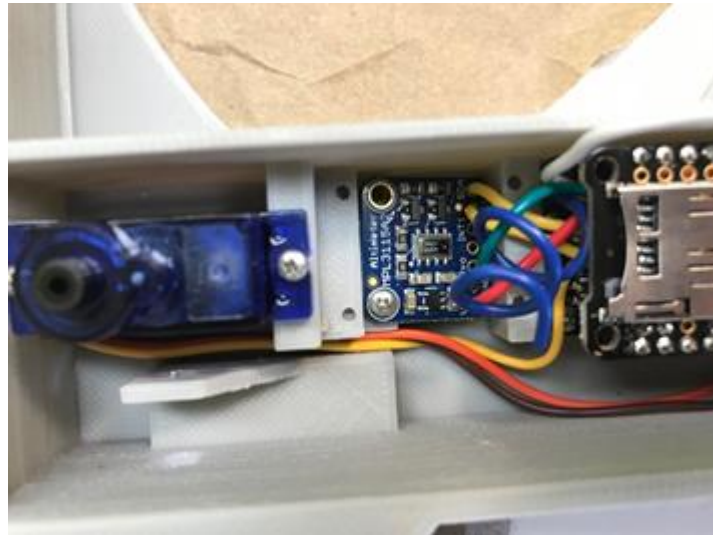


Figure A4: The MPL3115A2 sensor has been placed into position.



Figure A5: The SPDT slide switch used to power the instrument on and off has been put into place.



Figure A6: The arm is put in place with the spring, clevis, and cotter pin.

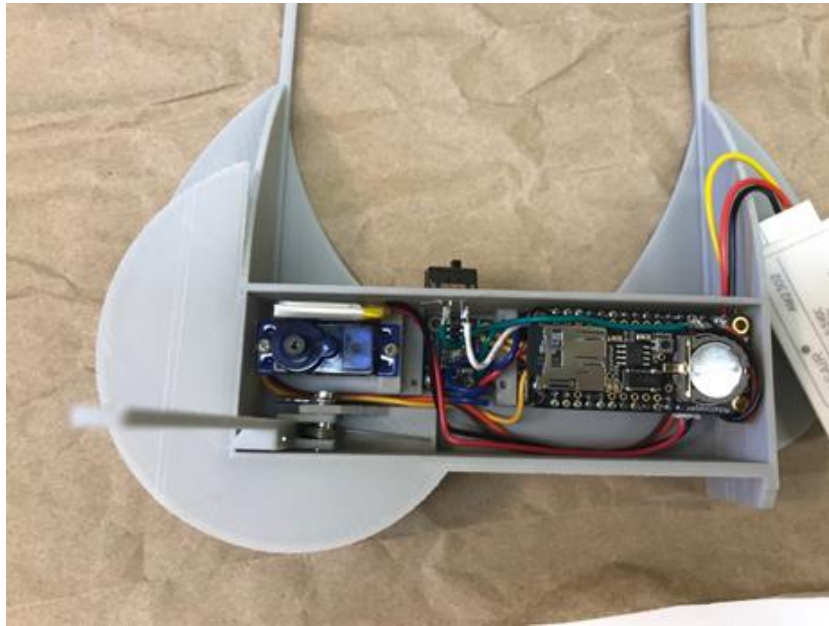


Figure A7: The batteries are put in place. Note that this version of the mini-GNI does not have a BNO055 sensor, which would be placed just above the MPL3115A2 sensor.



Figure A8: The door is screwed into place to the Micro Servo. The AM2302 sensor is attached to the side via adhesive putty as seen in Figure 5.

The mini-GNI control station is made of components detailed in Table A2. It is assembled by attaching the Feather M0 to the TFT FeatherWing with male headers.

Part Name	Adafruit Part Number
Adafruit Feather M0 with RFM95 LoRa Radio	3178
TFT FeatherWing - 2.4" 320x420 Touchscreen	3315
Lithium Ion Polymer Battery - 3.7V 350mAh	2750

Table A2: Adafruit parts list for building the mini-GNI control station.

7.3 Mini-GNI Software

Software logic diagrams are provided for the mini-GNI (Figure A9) and its control station (Figure A10).

The full details of the software can be found at a GitHub repository: <https://github.com/nugentlab/miniGNI>.

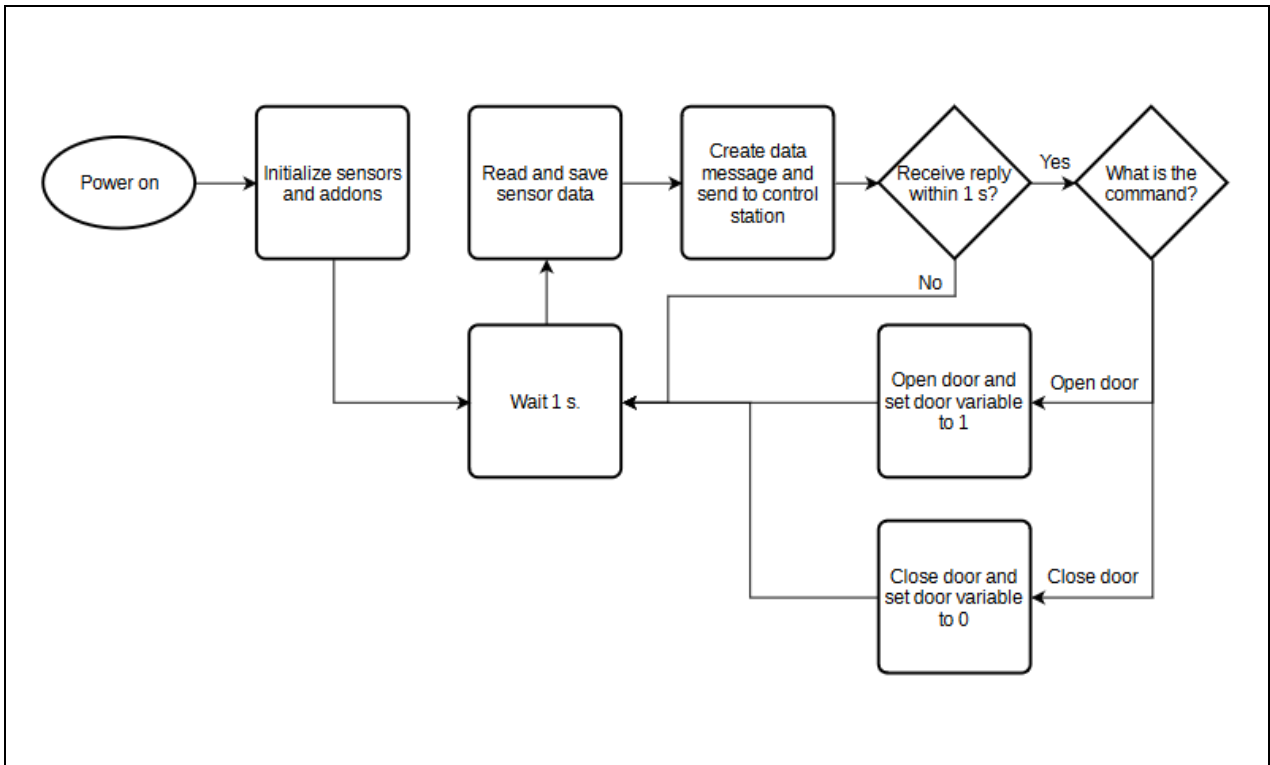


Figure A9: The software logic diagram for the mini-GNI. Every ~2-3 seconds, the mini-GNI reads sensor data and saves it. It also sends data for viewing to the ground control station. If it receives a message from the user at the control station, it opens and closes its door to expose and withdraw the polycarbonate slide for SSA impaction.

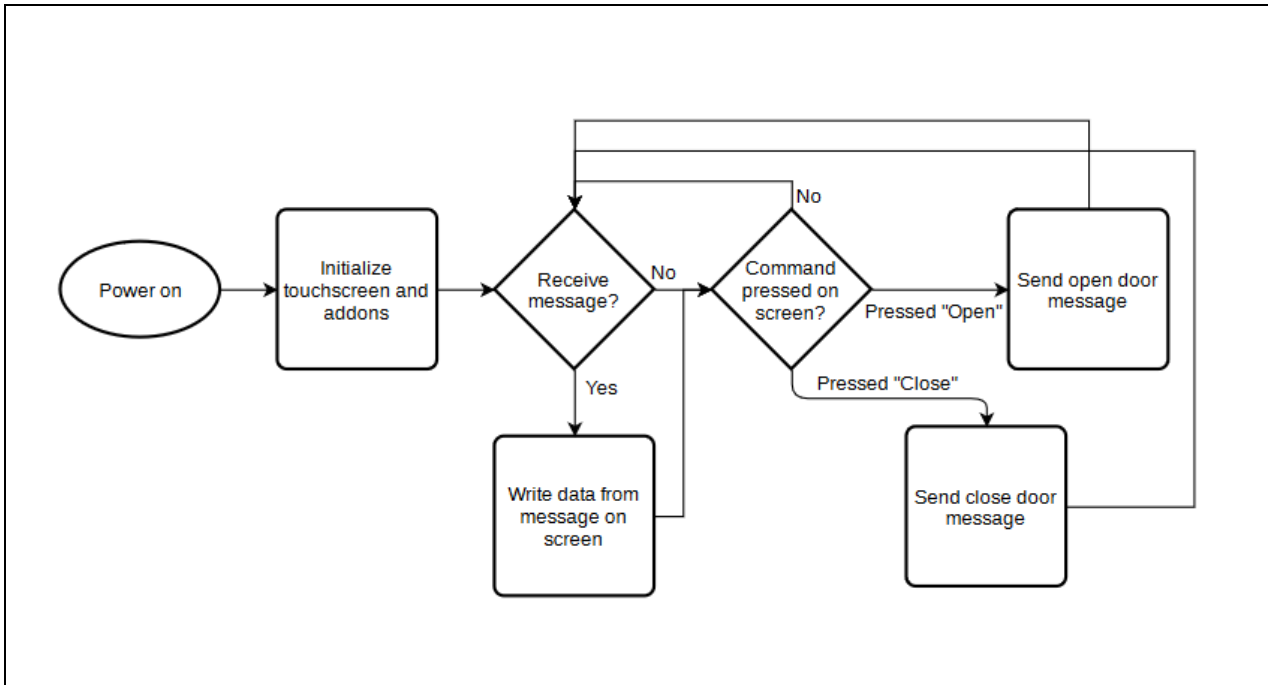


Figure A10: The software logic diagram for the mini-GNI control station. It receives information from the mini-GNI and displays it on the touchscreen. If the “open” or “close” commands are touched, the control station sends a message to the mini-GNI ordering it to open or close.